

# Can galactic outflows explain the properties of $\text{Ly}\alpha$ emitters?

Alvaro Orsi<sup>1,2,3\*</sup>, Cedric G. Lacey<sup>3</sup> and Carlton M. Baugh<sup>3</sup>

*1. Departamento de Astronomía y Astrofísica, Pontificia Universidad Católica, Av. Vicuña Mackenna 4860, Santiago, Chile.*

*2. Centro de Astro-Ingeniería, Pontificia Universidad Católica, Av. Vicuña Mackenna 4860, Santiago, Chile.*

*3. Institute for Computational Cosmology, Department of Physics, University of Durham, South Road, Durham DH1 3LE, UK.*

27 October 2011

## ABSTRACT

We study the properties of  $\text{Ly}\alpha$  emitters in a cosmological framework by computing the escape of  $\text{Ly}\alpha$  photons through galactic outflows. We combine the GALFORM semi-analytical model of galaxy formation with a Monte Carlo  $\text{Ly}\alpha$  radiative transfer code. The properties of  $\text{Ly}\alpha$  emitters at  $0 < z < 7$  are predicted using two outflow geometries: a Shell of neutral gas and a Wind ejecting material, both expanding at constant velocity. We characterise the differences in the  $\text{Ly}\alpha$  line profiles predicted by the two outflow geometries in terms of their width, asymmetry and shift from the line centre for a set of outflows with different hydrogen column densities, expansion velocities and metallicities. In general, the  $\text{Ly}\alpha$  line profile of the Shell geometry is broader and more asymmetric, and the  $\text{Ly}\alpha$  escape fraction is lower than with the Wind geometry for the same set of parameters. In order to implement the outflow geometries in the semi-analytical model GALFORM, a number of free parameters in the outflow model are set by matching the luminosity function of  $\text{Ly}\alpha$  emitters over the whole observed redshift range. The resulting neutral hydrogen column densities of the outflows for observed  $\text{Ly}\alpha$  emitters are predicted to be in the range  $\sim 10^{18} - 10^{23} [\text{cm}^{-2}]$ . The models are consistent with the observationally inferred  $\text{Ly}\alpha$  escape fractions, equivalent width distributions and with the shape of the  $\text{Ly}\alpha$  line from composite spectra. Interestingly, our predicted UV luminosity function of  $\text{Ly}\alpha$  emitters and the fraction of  $\text{Ly}\alpha$  emitters in Lyman-break galaxy samples at high redshift are in partial agreement with observations. Attenuation of the  $\text{Ly}\alpha$  line by the presence of a neutral intergalactic medium at high redshift could be responsible for this disagreement. We predict that  $\text{Ly}\alpha$  emitters constitute a subset of the galaxy population with lower metallicities, lower instantaneous star formation rates and larger sizes than the overall population at the same UV luminosity.

**Key words:** galaxies:high-redshift – galaxies:evolution – cosmology:large scale structure – methods:numerical

## 1 INTRODUCTION

Over the past 10 years the  $\text{Ly}\alpha$  line has proved to be a successful tracer of galaxies in the redshift range  $2 < z < 7$  (e.g. Cowie & Hu 1998; Kudritzki et al. 2000; Rhoads et al. 2000; Hu et al. 2002; Gronwall et al. 2007; Ouchi et al. 2008; Nilsson et al. 2009; Shimasaku et al. 2006; Kashikawa et al. 2006; Hu et al. 2010; Guaita et al. 2010). More recently, samples of  $\text{Ly}\alpha$  emitters at  $z \sim 0.2$  obtained with the GALEX satellite (Deharveng et al. 2008; Cowie, Barger & Hu 2010), have allowed us to study this galaxy population over an even broader range of redshifts.

Star-forming galaxies emit  $\text{Ly}\alpha$  radiation when ionizing photons produced by massive young stars are absorbed by atomic hydrogen (HI) regions in the interstellar medium (ISM). These hy-

drogen atoms then recombine leading to the emission of  $\text{Ly}\alpha$  photons. Therefore,  $\text{Ly}\alpha$  emission is, in principle, closely related to the star formation rate (SFR) of galaxies. However, in general only a small fraction of  $\text{Ly}\alpha$  photons manage to escape from galaxies (e.g. Hayes et al. 2011). This makes it difficult to relate  $\text{Ly}\alpha$  emitters to other star forming galaxy populations at high redshift, such as Lyman-break galaxies (LBGs) or sub-millimetre galaxies (SMGs).

The physical properties of galaxies selected by their  $\text{Ly}\alpha$  emission are inferred from spectral and photometric data (Gawiser et al. 2007; Gronwall et al. 2007; Nilsson et al. 2009; Guaita et al. 2011). Furthermore,  $\text{Ly}\alpha$  emitters are currently used to study the kinematics of the ISM in high redshift galaxies (Shapley et al. 2003; Steidel et al. 2010, 2011; Kulas et al. 2011), to trace the large scale structure of the Universe (Shimasaku et al. 2006; Gawiser et al. 2007; Kovač et al. 2007; Orsi et al. 2008; Francke 2009; Ouchi et al. 2010), to constrain the epoch of reionization (Kashikawa et al. 2006; Dayal, Maselli & Ferrara

\* Email: aaorsi@astro.puc.cl

2011; Ouchi et al. 2010; Stark et al. 2010; Schenker et al. 2011; Pentericci et al. 2011) and to test galaxy formation models (Le Delliou et al. 2005, 2006; Kobayashi, Totani & Nagashima 2007; Nagamine et al. 2010; Dayal, Ferrara & Saro 2010).

Despite this progress, understanding the physical mechanisms which drive the escape of Ly $\alpha$  radiation from a galaxy remains a challenge. Ly $\alpha$  photons undergo resonant scattering when interacting with hydrogen atoms, resulting in an increase of the path length that photons need to travel before escaping the medium. Therefore, the probability of photons being absorbed by dust grains is greatly enhanced, making the escape of Ly $\alpha$  photons very sensitive to even small amounts of dust. Furthermore, as a result of the complex radiative transfer, the frequency of the escaping Ly $\alpha$  photons generally departs from the line centre as a consequence of the large number of scatterings with many hydrogen atoms.

Recent observational studies have used various methods to infer the escape fraction of Ly $\alpha$  photons,  $f_{\text{esc}}$  (Atek et al. 2008, 2009; Östlin et al. 2009; Kornei et al. 2010; Hayes et al. 2010, 2011). This is generally done either by comparing the observed line ratio between Ly $\alpha$  and other hydrogen recombination lines, such as H $\alpha$  and H $\beta$ , or by comparing the star formation rate derived from the Ly $\alpha$  luminosity to that obtained from the ultraviolet continuum. The first method is the more direct, since the intrinsic fluxes of the comparison lines can be inferred after correcting the observed fluxes for extinction. Then, the departure from case B recombination of the ratio of the Ly $\alpha$  intensity to another hydrogen recombination line is attributed to the escape fraction of Ly $\alpha$  differing from unity. The second method, on the other hand, relies heavily on the assumed stellar population model used, the choice of the stellar initial mass function (IMF) and the attenuation of the ultraviolet continuum by dust, and is therefore more uncertain.

These measurements have revealed that the escape fraction of Ly $\alpha$  emitters can be anything between  $10^{-3}$  and 1. The observational data listed above also suggest a correlation between the value of the escape fraction and the dust extinction. The large scatter found in this relation suggests there is a range of physical parameters which determine the value of  $f_{\text{esc}}$ .

Early theoretical models of Ly $\alpha$  emission from galaxies were based on a static ISM (see, e.g. Neufeld 1990; Charlot & Fall 1993). These models explained the difficulty of observing Ly $\alpha$  in emission due to its very high sensitivity to dust in such a medium. Moreover, the first observations of Ly $\alpha$  emission in local starburst dwarf galaxies suggested a strong correlation between metallicity and Ly $\alpha$  luminosity (Meier & Terlevich 1981; Hartmann, Huchra & Geller 1984; Hartmann et al. 1988), leading to the conclusion that metallicity, which supposedly traces the amount of dust in galaxies, is the most important factor driving the visibility of the Ly $\alpha$  line.

However, subsequent observational studies showed only a weak correlation between Ly $\alpha$  luminosity and metallicity, suggesting instead the importance of the neutral gas distribution and its kinematics (e.g., Giavalisco, Koratkar & Calzetti 1996). Further analysis of metal lines in local starbursts revealed the presence of outflows which allow the escape of Ly $\alpha$  photons. The observed asymmetric P-Cygni Ly $\alpha$  line profiles are consistent with Ly $\alpha$  photons escaping from an expanding shell of neutral gas (Thuan & Izotov 1997; Kunth et al. 1998; Mas-Hesse et al. 2003). This established outflows as the main mechanism responsible for the escape of Ly $\alpha$  photons from galaxies. Furthermore, observations at higher redshifts reveal Ly $\alpha$  line profiles which also resemble those expected when photons escape through a galactic

outflow (Shapley et al. 2003; Kashikawa et al. 2006; Kornei et al. 2010; Hu et al. 2010).

In the last few years there has been significant progress in the modelling of Ly $\alpha$  emitters in a cosmological setting. The first consistent hierarchical galaxy formation model which included Ly $\alpha$  emission is the one described by Le Delliou et al. (2005, 2006) and Orsi et al. (2008), which makes use of the GALFORM semi-analytical model. In this model, the simple assumption of a fixed escape fraction,  $f_{\text{esc}} = 0.02$ , regardless of any galaxy property or redshift, allowed us to predict remarkably well the abundances and clustering of Ly $\alpha$  emitters over a wide range of redshifts and luminosities.

Nagamine et al. (2006, 2010) modelled Ly $\alpha$  emitters in cosmological SPH simulations. In order to match the abundances of Ly $\alpha$  emitters at different redshifts, they were forced to introduce a tunable escape fraction and a duty cycle parameter. Kobayashi, Totani & Nagashima (2007, 2010) developed a simple phenomenological model to compute  $f_{\text{esc}}$  in a semianalytical model. Their analytical prescription for  $f_{\text{esc}}$  distinguishes between outflows produced in starbursts and static media in quiescent galaxies. Dayal et. al use an SPH simulation to study Ly $\alpha$  emitters at high redshift and their attenuation by the neutral intergalactic medium (IGM). However, they assume the Ly $\alpha$  escape fraction is related to the escape of UV continuum photons (Dayal, Ferrara & Gallerani 2008; Dayal, Ferrara & Saro 2010; Dayal, Maselli & Ferrara 2011). Tilvi et al. (2009, 2010) make predictions for Ly $\alpha$  emitters using an N-body simulation and the uncertain assumption that the Ly $\alpha$  luminosity is proportional to the halo mass accretion rate. More recently, Forero-Romero et al. (2011) presented a model for high redshift Ly $\alpha$  emitters based on a hydrodynamic simulation, approximating Ly $\alpha$  photons to escape from homogeneous and clumpy gaseous, static slabs.

Motivated by observational evidence showing that Ly $\alpha$  photons escape through outflows, we present a model that incorporates a more physical treatment of the Ly $\alpha$  propagation than previous work, whilst at the same time being computationally efficient, so as to allow its application to a large sample of galaxies at different redshifts.

Such a physical approach to modelling the escape of Ly $\alpha$  photons requires a treatment of the radiative transfer of photons through an HI region. The scattering and destruction of Ly $\alpha$  photons have been extensively studied due to their many applications in astrophysical media. Harrington (1973) studied analytically the emergent spectrum from an optically thick, homogeneous static slab with photons generated at the line centre. This result was generalised by Neufeld (1990), to include photons generated at any frequency, and to provide an analytical expression for  $f_{\text{esc}}$  in this configuration.

Numerical methods, on the other hand, allow us to study the line profiles and escape fractions of Ly $\alpha$  photons in a wider variety of configurations. The standard approach is to use a Monte Carlo algorithm, in which the paths of a set of photons are followed one at a time through many scattering events, until the photon either escapes or is absorbed by a dust grain. Such calculations have been applied successfully to study the properties of Ly $\alpha$  emitters in different scenarios (see, e.g. Ahn, Lee & Lee 2000; Zheng & Miralda-Escudé 2002; Ahn 2003, 2004; Verhamme, Schaerer & Maselli 2006; Dijkstra, Haiman & Spaans 2006; Laursen & Sommer-Larsen 2007; Laursen, Razoumov & Sommer-Larsen 2009).

Recently, Zheng et al. (2010, 2011) combined a Monte Carlo Ly $\alpha$  radiative transfer model with a cosmological reionization sim-

ulation at  $z \sim 6$ , obtaining extended Ly $\alpha$  emission due to spatial diffusion. Their simulation box is, however, too small to be evolved to the present day without density fluctuations becoming nonlinear on the box scale, and does not have a volume large enough to sample a wide range of environments.

Previous work has not studied Ly $\alpha$  emitters in a framework that at the same time spans the galaxy formation and evolution process over a broad range of redshifts and includes Ly $\alpha$  radiative transfer. The need for such hybrid approach is precisely the motivation for this paper.

Given the observational evidence that outflows facilitate the escape of Ly $\alpha$  photons from galaxies, here we study the nature of Ly $\alpha$  emitters by computing the escape of photons from galaxies in an outflow of material by using a Monte Carlo Ly $\alpha$  radiative transfer model. Galactic outflows in our model are defined according to predicted galaxy properties in a simple way. This makes our modelling feasible on a cosmological scale, whilst retaining all the complexity of Ly $\alpha$  radiative transfer. Following our previous work, we use the semianalytical model GALFORM. This paper represents a significant improvement over the treatment of Ly $\alpha$  emitters in hierarchical galaxy formation models initially described in Le Delliou et al. (2005, 2006) and Orsi et al. (2008), which all assumed a constant escape fraction.

The outline of this paper is as follows: Section 2 describes the galaxy formation and radiative transfer models used. Also, we describe the two versions of galactic outflow geometries we use and explain how these are constructed in terms of galaxy parameters that can be extracted from our semi-analytical model. In Section 3 we present the properties of the Ly $\alpha$  line profiles and escape fractions predicted by our outflow geometries. In Section 4 we describe the galaxy properties that are relevant to our Ly $\alpha$  modelling and describe how we combine the Ly $\alpha$  radiative transfer model with the semi-analytical model. In Section 5 we present our main results, where we compare with observational measurements whenever possible, spanning the redshift range  $0 < z < 7$ . In Section 6 we present the implications of our modelling for the properties of galaxies selected by their Ly $\alpha$  emission, compared to the bulk of the galaxy population. Finally, in Section 7 we discuss our main findings. In the Appendix we give details of the implementation of the Monte Carlo radiative transfer model, the effect of the UV background on the outflow geometries and the numerical strategy followed to compute the escape fraction of Ly $\alpha$  photons from galaxies.

## 2 MODEL DESCRIPTION

Our approach to modelling Ly $\alpha$  emitters in a cosmological framework involves combining two independent codes. The backbone of our calculation is the GALFORM semi-analytical model of galaxy formation, outlined in Section 2.1, from which all relevant galaxy properties can be obtained, including the intrinsic Ly $\alpha$  luminosity. The second is the Monte Carlo Ly $\alpha$  radiative transfer code to compute both the frequency distribution of Ly $\alpha$  photons and the Ly $\alpha$  escape fraction. This code is described briefly in Section 2.2, with further information and tests presented in Appendix A. In Section 2.3 we describe the outflow geometries and the way these are defined in terms of galaxy properties.

### 2.1 Galaxy formation model

We use the semi-analytical model of galaxy formation, GALFORM, to predict the properties of galaxies and their abundance as a function of redshift. The GALFORM model is fully described in Cole et al. (2000) and Benson et al. (2003) (see also the review by Baugh 2006). The variant used here was introduced by Baugh et al. (2005), and is also described in detail in Lacey et al. (2008). The model computes star formation and galaxy merger histories for the whole galaxy population, following the hierarchical evolution of the host dark matter haloes.

The Baugh et al. (2005) model used here is the same GALFORM variant used in our previous work on Ly $\alpha$  emitters (Le Delliou et al. 2005, 2006; Orsi et al. 2008). A critical assumption of the Baugh et al. (2005) model is that stars which form in starbursts have a top-heavy initial mass function (IMF). The IMF is given by  $dN/d\ln(m) \propto m^{-x}$  with  $x = 0$  in this case. Stars formed quiescently in discs have a solar neighbourhood IMF, with the form proposed by Kennicutt (1983) with  $x = 0.4$  for  $m < 1M_{\odot}$  and  $x = 1.5$  for  $m > 1M_{\odot}$ . Both IMFs cover the mass range  $0.15M_{\odot} < m < 125M_{\odot}$ . Within the framework of  $\Lambda$ CDM, Baugh et al. argued that the top-heavy IMF is essential to match the counts and redshift distribution of galaxies detected through their sub-millimetre emission, whilst retaining the match to galaxy properties in the local Universe, such as the optical and far-IR luminosity functions, galaxy gas fractions and metallicities. Lacey et al. (2008) showed that the model predicts galaxy evolution in the IR in good agreement with observations from *Spitzer*. Moreover, Lacey et al. (2011) also showed that the Baugh et al. model predicts the abundance of Lyman-break galaxies (LBGs) remarkably well over the redshift range  $3 < z < 10$  (see also Gonzalez et al. 2011).

In GALFORM, the suppression of gas cooling from ionizing radiation produced by stars and active galactic nuclei (AGNs) during the epoch of reionization is modelled in a simple way: after the redshift of reionization, taken to be  $z_{\text{reion}} = 10$ , photoionization of the IGM completely suppresses the cooling and collapse of gas in haloes with circular velocities below  $V_{\text{crit}} = 30[\text{km/s}]$ .

The Baugh et al. model assumes two distinct modes of feedback from supernovae, a *reheating mode*, in which cold gas is expelled back to the hot halo, and a *superwind mode*, in which cold gas is ejected out of the galaxy halo. We describe both modes of supernova feedback in more detail in section 2.3.2 (see also Lacey et al. 2008).

Unlike the Bower et al. (2006) variant of GALFORM, the model used here does not incorporate feedback from an AGN. The superwind mode of feedback produces similar consequences to the quenching of gas cooling by the action of an AGN, as both mechanisms suppress the bright end of the LF. However, the Bower et al. (2006) model does not reproduce the observed abundances of LBGs or submillimetre galaxies (SMGs) at high redshift, which span a redshift range which overlaps with that of the LFs of Ly $\alpha$  emitters considered in this paper. Therefore, we do not use this GALFORM variant to make predictions for Ly $\alpha$  emitters.

In GALFORM, the intrinsic Ly $\alpha$  emission is computed as follows:

- (i) The composite stellar spectrum of the galaxy is calculated, based on its predicted star formation history, including the effect of the metallicity with which new stars are formed, and taking into account the IMFs adopted for different modes of star formation.
- (ii) The rate of production of Lyman continuum (Lyc) photons is computed by integrating over the composite stellar spectrum. We

assume that all of these ionizing photons are absorbed by neutral hydrogen within the galaxy. The mean number of Ly $\alpha$  photons produced per Ly $\gamma$  photon, assuming a gas temperature of  $10^4$  K for the ionized gas, is approximately 0.677, assuming Case B recombination (Osterbrock 1989).

(iii) The observed Ly $\alpha$  flux depends on the fraction of Ly $\alpha$  photons which escape from the galaxy ( $f_{\text{esc}}$ ). Previously we assumed this to be constant and independent of galaxy properties. The escape fraction was fixed at  $f_{\text{esc}} = 0.02$ , resulting in a remarkably good match to the observed Ly $\alpha$  LFs over the redshift range  $3 < z < 6$ . In our new model, we make use of a Monte Carlo radiative transfer model of Ly $\alpha$  photons to compute  $f_{\text{esc}}$  in a more physical way. This model is briefly described in the next subsection.

## 2.2 Monte Carlo Radiative Transfer Model

In order to compute the Ly $\alpha$  escape fraction and line profile we construct a Monte Carlo radiative transfer model for Ly $\alpha$  photons. This simulates the escape of a set of photons from a source as they travel through an expanding HI region, which may contain dust, by following the scattering histories of individual photons. By following a large number of photons we can compute properties such as the Ly $\alpha$  spectrum and the escape fraction.

Our Monte Carlo radiative transfer code works on a 3D grid in which each cell contains information about the neutral hydrogen density,  $n_H$ , the temperature of the gas,  $T$ , and the bulk velocity,  $v_{\text{bulk}}$ . Once a Ly $\alpha$  photon is created, a random direction and frequency are assigned to it, and the code follows its trajectory and computes each scattering event of the photon as it crosses the HI region until it either escapes or is absorbed by a dust grain. If the photon escapes, then its final frequency is recorded, a new photon is generated and the procedure is repeated.

Clearly, to get an accurate description of the escape of Ly $\alpha$  photons from a given geometrical setup, many photons must be followed. The number of photons needed to achieve convergence will depend on the properties of the medium, but also on the quantity in which we are interested. For example, for most of the outflows studied here, only a few thousand photons are needed to compute an accurate escape fraction. However, tens of thousand of photons are needed to obtain a smooth line profile.

Our radiative transfer model of Ly $\alpha$  photons is similar to previous models in the literature (e.g. Zheng & Miralda-Escudé 2002; Ahn 2003, 2004; Verhamme, Schaerer & Maselli 2006; Dijkstra, Haiman & Spaans 2006; Laursen, Razoumov & Sommer-Larsen 2009; Barnes & Haehnelt 2010). We describe the numerical implementation of our Monte Carlo model and the validation tests applied to it in Appendix A.

## 2.3 Outflow geometries

In our model, the physical conditions in the medium used to compute the escape of Ly $\alpha$  photons depend on several properties of galaxies predicted by GALFORM. Below we describe two outflow geometries for the HI region surrounding the source of Ly $\alpha$  photons. They differ in their geometry and the way the properties of galaxies from GALFORM are used. We assume the temperature of the medium to be constant at  $T = 10^4$  K, which sets the thermal velocity dispersion of atoms, following a Maxwell-Boltzmann distribution, to be  $v_{\text{th}} = 12.85 \text{ km s}^{-1}$  (see Eq. A1 in Appendix A for

more details). For simplicity, the source of Ly $\alpha$  photons is taken to be at rest in the frame of the galaxy, in the centre of the outflow, and emits photons at the line centre only,  $\lambda = 1215.68 \text{ \AA}$ .

### 2.3.1 Expanding thin shell

Previous radiative transfer studies of Ly $\alpha$  line profiles adopted an expanding shell in the same way as we used here (see, e.g. Ahn 2003, 2004; Verhamme, Schaerer & Maselli 2006; Schaerer 2007; Verhamme et al. 2008, and references therein). This model, hereafter named “Shell”, consists of a homogeneous, expanding, isothermal spherical shell, in which dust and gas are uniformly mixed. The shell, although thin, is described by an inner and outer radius  $R_{\text{in}}$  and  $R_{\text{out}}$ , which satisfy  $R_{\text{in}} = f_{\text{th}} R_{\text{out}}$ . We set  $f_{\text{th}} = 0.9$ . In addition, the medium is assumed to be expanding radially with constant velocity  $V_{\text{exp}}$ . The column density through the Shell is given by

$$N_H(r) = \frac{X_H M_{\text{shell}}}{4\pi m_H R_{\text{out}}^2}, \quad (1)$$

where  $X_H = 0.74$  is the fraction of hydrogen in the cold gas and  $m_H$  is the mass of a hydrogen atom. In GALFORM, the Ly $\alpha$  luminosity originates in the disk (in quiescent galaxies) or the bulge (in starbursts). Some galaxies may also have contributions from both components. Therefore,  $M_{\text{shell}}$ ,  $R_{\text{out}}$  and  $V_{\text{exp}}$  are taken to be proportional to the mass of cold gas  $M_{\text{cold}}$ , half-mass radius  $R_{1/2}$  and circular velocity  $V_{\text{circ}}$ , respectively, i.e.,

$$M_{\text{shell}} = f_M \langle M_{\text{gas}} \rangle, \quad (2)$$

$$R_{\text{out}} = f_R \langle R_{1/2} \rangle, \quad (3)$$

$$V_{\text{exp}} = f_V \langle V_{\text{circ}} \rangle, \quad (4)$$

where  $f_M$ ,  $f_R$  and  $f_V$  are free parameters. To take into account the contribution from both components of a galaxy, we define

$$\langle M_{\text{gas}} \rangle = F_{\text{Ly}\alpha}^{\text{disk}} M_{\text{gas}}^{\text{disk}} + (1 - F_{\text{Ly}\alpha}^{\text{disk}}) M_{\text{gas}}^{\text{bulge}}, \quad (5)$$

$$\langle R_{1/2} \rangle = F_{\text{Ly}\alpha}^{\text{disk}} R_{1/2}^{\text{disk}} + (1 - F_{\text{Ly}\alpha}^{\text{disk}}) R_{1/2}^{\text{bulge}}, \quad (6)$$

$$\langle V_{\text{circ}} \rangle = F_{\text{Ly}\alpha}^{\text{disk}} V_{\text{circ}}^{\text{disk}} + (1 - F_{\text{Ly}\alpha}^{\text{disk}}) V_{\text{circ}}^{\text{bulge}}, \quad (7)$$

$$F_{\text{Ly}\alpha}^{\text{disk}} \equiv \frac{L_{\text{Ly}\alpha}^{\text{disk}}}{L_{\text{Ly}\alpha}^{\text{total}}}. \quad (8)$$

In each term, the superscript indicates the contribution from the disk, the bulge or the total (the sum of the two). In most galaxies, however, either the disk or bulge term completely dominates.

Likewise, the metallicity of the shell  $Z_{\text{out}}$  is taken to be the metallicity of the cold gas  $Z_{\text{cold}}$  weighted by a combination of the mass of cold gas and the Ly $\alpha$  luminosity of each component, i.e.,

$$Z_{\text{out}} = \frac{M_{\text{gas}}^{\text{disk}} L_{\text{Ly}\alpha}^{\text{disk}} Z_{\text{cold}}^{\text{disk}} + M_{\text{gas}}^{\text{bulge}} L_{\text{Ly}\alpha}^{\text{bulge}} Z_{\text{cold}}^{\text{bulge}}}{M_{\text{gas}}^{\text{disk}} L_{\text{Ly}\alpha}^{\text{disk}} + M_{\text{gas}}^{\text{bulge}} L_{\text{Ly}\alpha}^{\text{bulge}}}. \quad (9)$$

In order to compute the dust content in the outflow we assume that the mass of dust in the outflow,  $M_{\text{dust}}$ , is proportional to the gas mass and metallicity, i.e.

$$M_{\text{dust}} = \frac{\delta_*}{Z_{\odot}} M_{\text{shell}} Z_{\text{out}}, \quad (10)$$

where the dust-to-gas ratio is taken to be  $\delta_* = 1/110$  at the solar metallicity  $Z_{\odot} = 0.02$  (Granato et al. 2000). The extinction optical depth at the wavelength of Ly $\alpha$  can be written as

$$\tau_d = \frac{E_{\odot}}{Z_{\odot}} N_H Z_{\text{out}}, \quad (11)$$

where  $E_{\odot} = 1.77 \times 10^{-21} [\text{cm}^2]$  is the ratio  $\tau_d/N_H$  for solar metallicity at the wavelength of Ly $\alpha$  (1216 Å). Throughout this work we use the extinction curve and albedo from Silva et al. (1998), which are fit to the observed extinction and albedo in the Galactic ISM. For a dust albedo  $A$ , the optical depth for absorption is simply

$$\tau_a = (1 - A)\tau_d. \quad (12)$$

At the wavelength of Ly $\alpha$ ,  $A_{Ly\alpha} = 0.39$ .

### 2.3.2 Galactic Wind

Supernovae heat and accelerate the ISM through shocks and hence generate outflows from galaxies (see, e.g. Frank 1999; Strickland 2002). Here we develop an outflow model, hereafter called “Wind”, which relates the density of the outflow to the mass ejection rate from galaxies due to supernovae. In GALFORM, this mass ejection rate is given by

$$\dot{M}_{\text{ej}} = [\beta_{\text{reh}}(V_{\text{circ}}) + \beta_{\text{sw}}(V_{\text{circ}})] \psi, \quad (13)$$

where

$$\beta_{\text{reh}} = \left( \frac{V_{\text{circ}}}{V_{\text{hot}}} \right)^{-\alpha_{\text{hot}}}, \quad (14)$$

$$\beta_{\text{sw}} = f_{\text{sw}} \min[1, (V_{\text{circ}}/V_{\text{sw}})^{-2}]. \quad (15)$$

The terms  $\beta_{\text{reh}}$  and  $\beta_{\text{sw}}$  define the two different modes of supernova feedback (the *reheating* and *superwind*), and the constants  $\alpha_{\text{hot}}$ ,  $V_{\text{hot}}$ ,  $f_{\text{sw}}$  and  $V_{\text{sw}}$  are free parameters of GALFORM, chosen by fitting the model predictions to observed galaxy LFs. The instantaneous star formation rate,  $\psi$  is obtained as

$$\psi = \frac{M_{\text{gas}}}{\tau_*}, \quad (16)$$

where  $\tau_*$  is the star formation time-scale, which is different for quiescent galaxies and starbursts. For a detailed description of the star formation and supernova feedback processes in this variant of GALFORM, see Baugh et al. (2005) and Lacey et al. (2008). Since star formation can occur in the disk and in the bulge, there is a mass ejection rate term  $\dot{M}_{\text{ej}}$  associated with each component.

We construct the wind as an isothermal, spherical flow expanding at constant velocity  $V_{\text{exp}}$ , and inner radius  $R_{\text{wind}}$  (the wind is empty inside). In a steady-state spherical wind, the mass ejection rate is related to the velocity and density at any point of the Wind via the equation of mass continuity, i.e.

$$\dot{M}_{\text{ej}} = 4\pi r^2 V_{\text{exp}} \rho(r), \quad (17)$$

where  $\rho(r)$  is the mass density of the medium, and  $V_{\text{exp}}$  is calculated following equation (4). Since star formation in GALFORM can occur in both the disk and bulge of galaxies,  $\dot{M}_{\text{ej}}$  in equation (17) corresponds to the sum of the ejection rate from the disk and the bulge.

Following equation (17), the number density profile  $n_{HI}(r)$  in the Wind geometry varies according to

$$n_{HI}(r) = \begin{cases} 0 & r < R_{\text{wind}} \\ \frac{X_H \dot{M}_{\text{ej}}}{4\pi m_H r^2 V_{\text{exp}}} & r \geq R_{\text{wind}}. \end{cases} \quad (18)$$

The column density  $N_H$  of the outflow is

$$N_H = \frac{X_H \dot{M}_{\text{ej}}}{4\pi m_H R_{\text{wind}} V_{\text{exp}}}, \quad (19)$$

where the inner radius of the wind,  $R_{\text{wind}}$ , is computed in an analogous way to  $R_{\text{out}}$  in the Shell geometry (Eq. 3). Note that both  $f_R$  and  $f_V$  in this case are different free parameters and independent of those used in the Shell geometry. The metallicity of the Wind,  $Z_{\text{wind}}$ , corresponds to the metallicity of the cold gas in the disk and bulge weighted by their respective mass ejection rates.

For computational reasons, the radiative transfer code requires us to define an outer radius,  $R_{\text{outer}}$ , for the Wind. However, since the number density of atoms decreases as  $\sim r^{-2}$ , we expect that at some point away from the centre the optical depth becomes so small that the photons will be able to escape regardless of the exact extent of the outflow. We find that an outer radius  $R_{\text{outer}} = 20R_{\text{wind}}$  yields converged results, i.e. the escape fraction of Ly $\alpha$  photons does not vary if we increase the value of  $R_{\text{outer}}$  further.

## 3 OUTFLOW PROPERTIES

In this section we explore the properties of the Ly $\alpha$  radiative transfer in our outflow geometries prior to coupling these to the galaxy formation model GALFORM. We do this by running our Monte Carlo radiative transfer model over a grid of configurations spanning a wide range of hydrogen column densities, expansion velocities and metallicities. In order to obtain well-defined Ly $\alpha$  line profiles, we run each configuration using  $5 \times 10^4$  photons. Therefore, the minimum Ly $\alpha$  escape fraction our models can compute in this case is  $f_{\text{esc}} = 2 \times 10^{-5}$ .

### 3.1 Ly $\alpha$ line properties

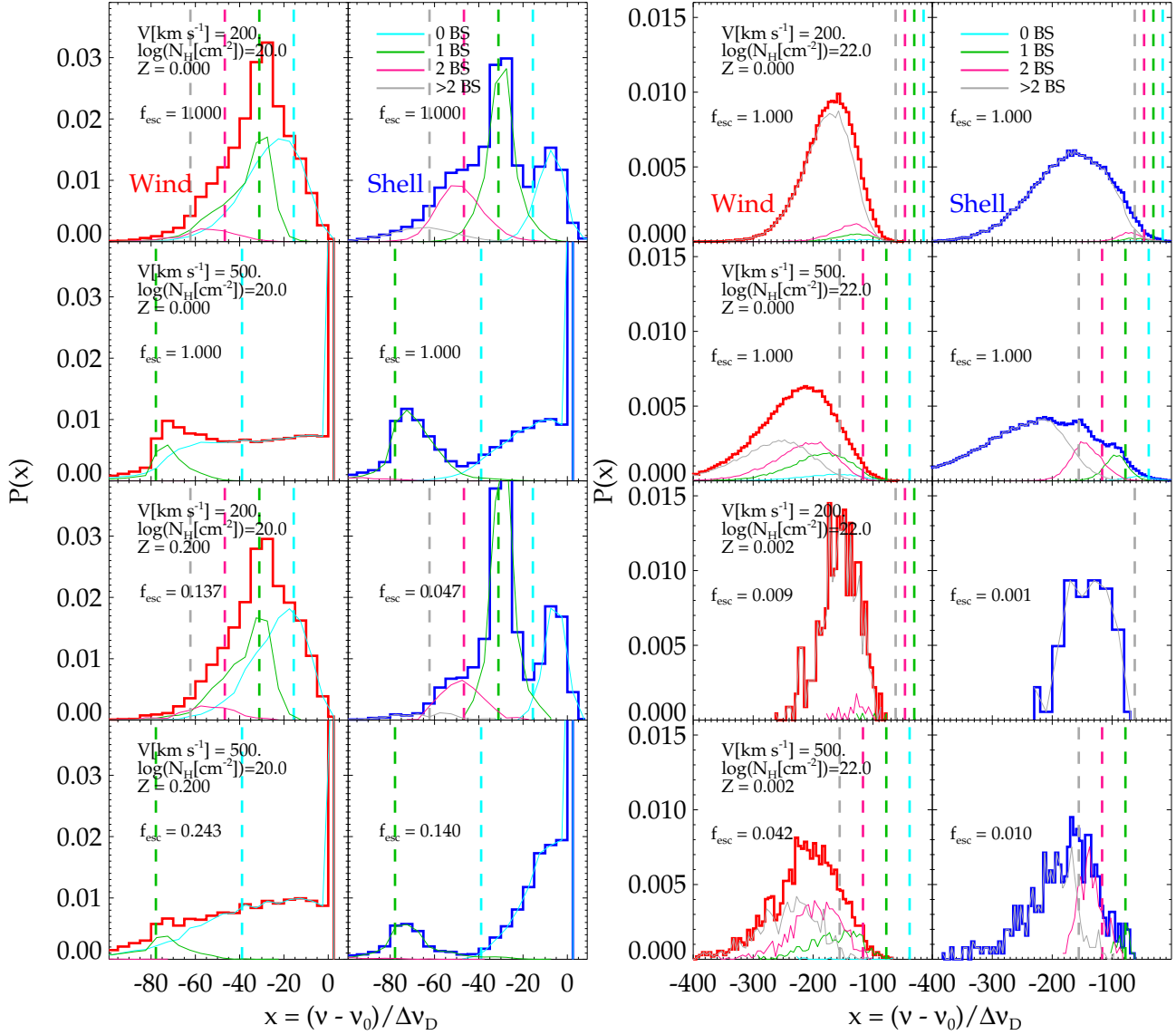
One important difference between our two outflow geometries is the way the column densities are computed. In the Shell geometry the column density is a function of the total cold gas mass of a galaxy and its size, whereas in the Wind geometry it depends on the mass ejection rate given by the supernova feedback model along with the size and the circular velocity of the galaxy. This difference translates into different predicted properties for Ly $\alpha$  emitters, as will be shown in the next section. However, even when the column density, velocity of expansion and outflow metallicity are the same, the two models will give different escape fractions and line profile shapes due to their different geometries.

Fig. 1 shows the Ly $\alpha$  line profiles obtained with the two models when matching the key properties for outflows at the same column densities. In order to make a fair comparison between the Shell and Wind geometries, we compare configurations with the same column density, expansion velocity and metallicity. In addition, the inner radius in the Wind geometry is chosen to be the same as its counterpart, the outer radius in the Shell geometry. The two panels of Fig. 1 display a set of configurations with column densities of  $N_H = 10^{20} [\text{cm}^{-2}]$  (left panel) and  $N_H = 10^{22} [\text{cm}^{-2}]$  (right panel). In the following, we express the photon’s frequency in terms of  $x$ , the shift in frequency around the line centre  $\nu_0$ , in units of the thermal width, i.e.

$$x \equiv \frac{(\nu - \nu_0)}{\Delta\nu_D}, \quad (20)$$

where  $\Delta\nu_D = v_{\text{th}}\nu_0/c$ , and  $c$  is the speed of light, and  $v_{\text{th}}$  is the thermal velocity discussed in Section 2.3.

As a general result, outflows with a column density of  $N_H = 10^{20} [\text{cm}^{-2}]$ , regardless of the other properties, produce multiple peaks at frequencies redward of the line centre in both geometries, with different levels of asymmetry. The Shell geometry generates



**Figure 1.** Comparison of the Ly $\alpha$  line profile obtained with the Wind and Shell geometries for  $N_H = 10^{20} [\text{cm}^{-2}]$  (leftmost two columns) and  $N_H = 10^{22} [\text{cm}^{-2}]$  (rightmost two columns). The red (blue) histogram shows the full spectrum obtained for the Wind (Shell) outflow geometry. The cyan, green, pink and gray lines show the spectra of photons which experienced 0, 1, 2 and 3 or more back-scatterings before escaping, respectively. Likewise, the same colours are used to plot vertical dashed lines showing the frequencies corresponding to  $-x_{bs}$ ,  $-2x_{bs}$ ,  $-3x_{bs}$  and  $-4x_{bs}$ , respectively (see text for details). Each row displays a different configuration, characterised by a given  $N_H$ ,  $V_{\text{exp}}$  and  $Z$ , as indicated in the legend. The top two rows correspond to dust-free configurations ( $Z = 0$ ), whereas the bottom two have different metallicities, chosen to have equal dust optical depth, although having different column densities of hydrogen. The escape fraction of Ly $\alpha$  photons,  $f_{\text{esc}}$ , is indicated in each box. The Ly $\alpha$  profiles shown are normalized to the total number of escaping photons (instead of the total number of photons run), to ease the comparison between the dusty and dust-free cases. Note the different range in the x-axis between the left and right panels.

more prominent peaks than the Wind geometry. The frequency of the main peak is, however, the same in both outflow geometries.

On the other hand, outflows with  $N_H = 10^{22} [\text{cm}^{-2}]$  display broader Ly $\alpha$  profiles. As opposed to the lower column density case, these profiles display a single peak, also redward of the line centre. The position of this peak is also the same for both geometries.

The effect of a large expansion velocity is shown in the 2nd and 4th rows in both panels of Fig. 1. Here the configurations have  $V_{\text{exp}} = 500 [\text{km/s}]$ . The differences with the configurations where  $V_{\text{exp}} = 200 [\text{km/s}]$  are evident: the profiles are broader, and the position of the peaks are displaced to redder frequencies. Furthermore, in the left panel of Fig. 1, where  $N_H = 10^{20} [\text{cm}^{-2}]$ , it is

shown that a significant fraction of photons escape at the line centre. The high expansion velocity in this case makes the medium optically thin, allowing many photons to escape without undergoing any scattering.

For the configurations with  $N_H = 10^{20} [\text{cm}^{-2}]$ , the optical depth that a photon at the line centre ( $x = 0$ ) sees when traveling along the radial direction is  $\tau_0 = 3.63$  and  $\tau_0 = 0.57$  for expansion velocities  $V_{\text{exp}} = 200 [\text{km/s}]$  and  $V_{\text{exp}} = 500 [\text{km/s}]$ , respectively. Accordingly, the configurations with  $N_H = 10^{22} [\text{cm}^{-2}]$  have optical depths a factor 100 higher. On the other hand, a static medium with  $N_H = 10^{20} [\text{cm}^{-2}]$  has a much higher optical depth,  $\tau_0 = 3.31 \times 10^6$ . This illustrates the strong effect of the expansion

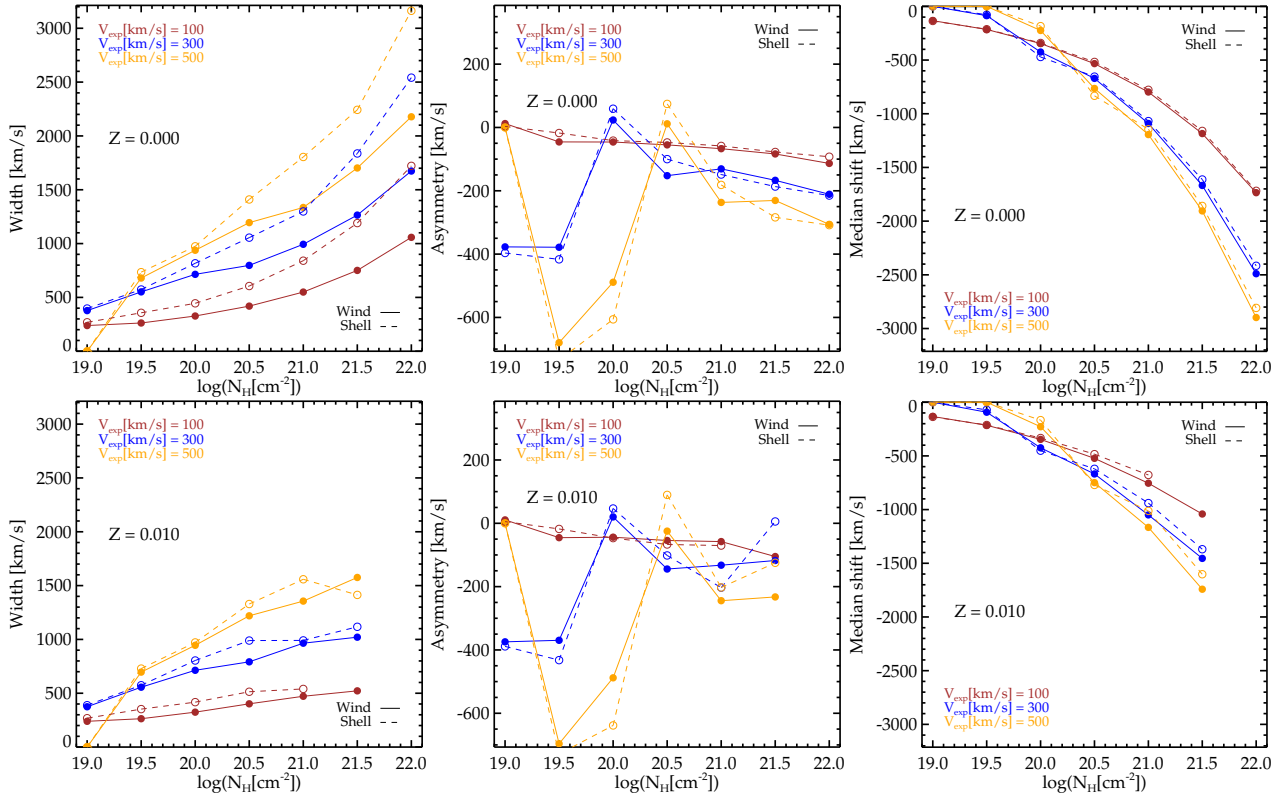


**Figure 2.** The properties of the Ly $\alpha$  profiles predicted by the two outflow geometries for a given column density, expansion velocity and metallicity. Left panels: the width of the profiles, defined as the difference between the 90 and 10 percentiles of the frequency distribution of escaping Ly $\alpha$  photons, measured in km/s. Middle panels: the asymmetry, defined in the text, and measured in km/s. Right panels: the shift of the median of the Ly $\alpha$  profiles with respect to the line centre, measured in km/s. Note that negative velocities indicate redshifting. The top row shows the Ly $\alpha$  profile properties in dust-free outflows. The bottom row shows outflows with a metallicity  $Z = 0.01$ . Different expansion velocities spanning the range 100 – 500 km/s are shown with different colours, as shown by the labels in each panel. The Wind geometry is shown with solid lines and filled circles. The Shell geometry is shown with dashed lines and open circles.

velocity in reducing the optical depth of the medium, thus allowing photons to escape.

The Ly $\alpha$  line profiles obtained can be characterised by the frequency distribution of photons split according to the number of backscatterings they experience before escaping (i.e. the number of times photons bounce back to the inner, empty region). When photons interact for the first time with the outflow, a fraction of them will experience a backscattering. These events are significant since the distribution of scattering angles is dipolar (see Eq. A13 in Appendix A). The frequency of a photon after a scattering event, in the observer’s frame, is given by Eq. (A15). Depending on the direction of the photon after the scattering event, its frequency will fall within the range  $x = [-2x_{bs}, 0]$ , where  $x_{bs} \equiv V_{\text{exp}}/v_{\text{th}}$  (see also Ahn 2003; Verhamme, Schaerer & Maselli 2006). Photons that do not experience a backscattering, or escape directly, form the cyan curves in Fig. 1. If the photon is backscattered exactly backwards, then its frequency will be  $x = -2x_{bs}$ . The cross-section for scattering is significantly reduced for these photons, and so a fraction escape without undergoing any further interaction with the outflow. Photons backscattered once form the green curves in Fig. 1. If a photon experiences a second backscatter in the exact opposite direction, then its frequency will become  $x = -4x_{bs}$ , and the cross-section for a further scattering will again reduce significantly. The magenta curves show the distribution of photons that experienced 2 backscatterings. Finally, photons that experience 3 or more backscatterings are shown in gray.

In detail, the geometrical differences between the Shell and Wind models are translated into each backscattering peak contributing in a different proportion and with a different shape to the overall spectrum for each geometry. Previous studies have also found this relation between the peaks of backscattered photons and  $x_{bs}$  in media with column densities of the order of  $N_H \sim 10^{20} [\text{cm}^{-2}]$  (Ahn 2003, 2004; Verhamme, Schaerer & Maselli 2006), although they did not study the line profiles for higher optical depths as we do here. For  $N_H = 10^{22} [\text{cm}^{-2}]$ , we find that the peaks are displaced considerably from their expected position based on the simple argument above. This is not surprising, since in outflows with very large optical depths the number of scatterings broadens the profiles and reddens the peak positions.

In the Wind geometry, the contribution of photons featuring no backscatterings dominates most of the total profile for  $N_H = 10^{20} [\text{cm}^{-2}]$ , whereas in the overall line profile for the Shell geometry there is a clear distinction between a region dominated by photons suffering no backscatterings and those backscattered once (green curve). This illustrates again how the Ly $\alpha$  line profile in the Shell geometry features clear multiple peaks from one or more backscatterings, whereas in the Wind geometry the secondary peaks are less obvious.

Fig. 1 also shows the effect of including dust in the outflows. Overall, dust absorption has more effect on the redder side of the line profiles than at frequencies closer to the line centre, where the probability of scattering with hydrogen atoms is significantly



higher than the probability of interaction with dust. In detail, the sensitivity of Ly $\alpha$  photons to dust is the result of an interplay between the optical depths of hydrogen and dust at the photon frequency (the cross-section of scattering is significantly reduced away from the line centre, and hence so is the average number of scatterings) and the bulk velocity of the gas, reducing the number of scatterings further, and thus also the probability for a photon to be absorbed.

A less obvious outflow property for determining the Ly $\alpha$  attenuation by dust is its geometry. Despite the similarities between the outflow geometries, the Shell geometry consistently gives a lower Ly $\alpha$  escape fraction than the Wind geometry in the configurations studied in Fig. 1.

As a final comparison, in Fig. 1 we chose a metallicity of  $Z = 0.2$  for the configurations with  $N_H = 10^{20} [\text{cm}^{-2}]$  and  $Z = 0.002$  for the configurations with  $N_H = 10^{22} [\text{cm}^{-2}]$ . Although the metallicities are different, the optical depth of dust, given by Eq. (11), is the same in both cases,  $\tau_d = 1.77$ . By matching the optical depth of dust, we can study the effect of  $N_H$  on the Ly $\alpha$  escape fraction. Fig. 1 shows that even when the optical depth of dust is the same, outflows with  $N_H = 10^{22} [\text{cm}^{-2}]$  have Ly $\alpha$  escape fractions up to an order of magnitude lower than those with  $N_H = 10^{20} [\text{cm}^{-2}]$ . This occurs since, in the former case, the average number of scatterings is about two orders of magnitude larger than in the latter, and hence the probability of photons interacting with a dust grain increases accordingly. This illustrates the complexity of the Ly $\alpha$  radiative transfer process.

To gain more insight into the difference in the Ly $\alpha$  profiles generated by different configurations, we show in Fig. 2 a measure of the width, asymmetry and average frequency shift of the Ly $\alpha$  profiles for a set of configurations spanning a range of expansion velocities of  $V_{\text{exp}} [\text{km/s}] = 100 - 500$ , column densities  $N_H [\text{cm}^{-2}] = 10^{19} - 10^{22}$ , and also two metallicities,  $Z = 0$  and  $Z = 0.01$ . To measure the width of the profiles we compute the difference in frequency between the 90 and 10 percentiles, expressed in velocity units. The asymmetry is computed as the difference between the blue side of the profile,  $P_{90} - P_{50}$  and the red side,  $P_{50} - P_{10}$ , where  $P_{10}$ ,  $P_{50}$  and  $P_{90}$  are the 10, 50 (median) and 90 percentile of the frequency distribution. The shift of the median is simply the position of the median of the Ly $\alpha$  profiles in velocity units.

Overall, by examining the top and bottom rows of Fig. 2 it becomes clear that the width, asymmetry and median shift of the Ly $\alpha$  profiles are fairly insensitive to the presence of dust in both outflow geometries. The only important effect of dust is to limit the range of column densities where the Ly $\alpha$  profiles are appreciable. Configurations with  $\log(N_H [\text{cm}^{-2}]) > 21.5$  do not feature data points on the plot, since all photons used to compute the Ly $\alpha$  profiles were absorbed by dust in this case. The optical depth of absorption,  $\tau_a$ , increases in proportion with the column density, as shown by Eqs. (11) and (12).

The small contribution of dust in shaping the Ly $\alpha$  profiles limits the information that can be extracted observationally from the Ly $\alpha$  line profile. If the outflow geometries studied here are good approximations to the outflows in Ly $\alpha$  emitters, then the Ly $\alpha$  escape fraction cannot be usefully constrained by using the shape of the spectrum.

Despite the above, the shape of the Ly $\alpha$  profiles in our outflow geometries is sensitive to other properties. Fig. 2 shows a clear increase in the width of the Ly $\alpha$  profiles, with both increasing column density and expansion velocity. Also, the Shell geometry generates consistently broader profiles than the Wind geometry, for all

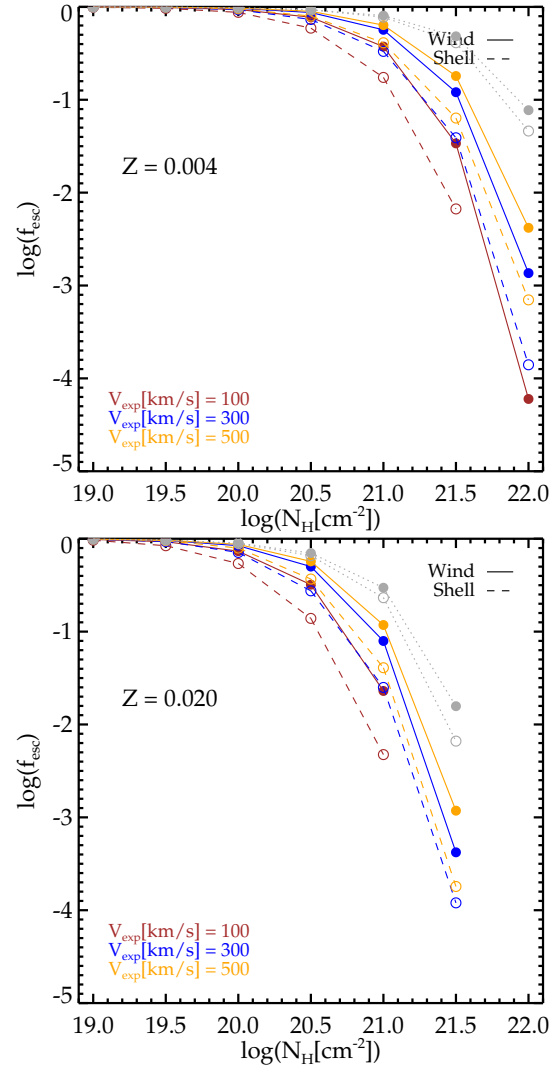


**Figure 3.** The Ly $\alpha$  escape fraction predicted by the two outflow geometries as a function of column density, expansion velocity and metallicity. The top panel shows configurations with  $Z = 0.004$ . In the bottom panel  $Z = 0.02$ . Expansion velocities spanning the range 100 – 500 km/s are shown with different colours, as shown in the legend of each box. The Wind geometry is shown with solid lines and filled circles. The Shell geometry is shown with dashed lines and open circles. The gray circles show the result of switching off the scattering of Ly $\alpha$  photons due to hydrogen atoms in the model, making photons interact only with dust grains.

the configurations studied. Note that this is illustrated in Fig. 1 as well.

The broadening of the Ly $\alpha$  profiles is, however, less evident in the configurations with  $N_H = 10^{19} [\text{cm}^{-2}]$ . At this low column density, and even at the lower expansion velocities, many photons manage to escape at the line centre without being scattered due to the reduced optical depth, as explained above. Hence, the Ly $\alpha$  profiles are narrower. In particular, the width of the Ly $\alpha$  profile, when  $N_H = 10^{19} [\text{cm}^{-2}]$  and  $V_{\text{exp}} = 500 [\text{km/s}]$  is zero, showing that nearly all photons escaped directly.

At higher column densities, the expansion velocity plays an increasingly important role at broadening the profiles. In the outflows with  $N_H = 10^{20} [\text{cm}^{-2}]$ , without dust, the width of the profiles increases from  $\sim 300 [\text{km/s}]$  to  $\sim 1000 [\text{km/s}]$  for expansion velocities of  $V_{\text{exp}} = 100 [\text{km/s}]$  and  $V_{\text{exp}} = 500 [\text{km/s}]$ , respec-



tively. When  $N_H = 10^{22} [\text{cm}^{-2}]$ , the width of the profile depends strongly on the geometry of the outflow. The width for the Wind geometry spans a range of  $\sim 1000 [\text{km/s}]$  to  $\sim 2200 [\text{km/s}]$  for expansion velocities of  $V_{\text{exp}} = 100 [\text{km/s}]$  and  $V_{\text{exp}} = 500 [\text{km/s}]$ , respectively, whereas for the Shell geometry it spans a much larger range of  $\sim 1700 [\text{km/s}]$  to  $\sim 3200 [\text{km/s}]$  for the same range of expansion velocities.

The effect of dust on the width of the profiles is negligible, except for the Shell geometry with  $N_H = 10^{21} [\text{cm}^{-2}]$ , where the width is reduced and is, therefore, closer to the width of the profiles of the Wind geometry.

The asymmetry of the profiles is somewhat more complicated to characterise in terms of the column density and expansion velocity of the outflows. As a general result, the Ly $\alpha$  profiles are asymmetric towards the red-side of the spectrum. This is not surprising, since atoms in an outflow “see” the Ly $\alpha$  photons redshifted, and the change in the direction of the photons due to the scattering event makes photons appear redder in the observer’s frame. Overall, as Fig. 2 shows, the asymmetry is larger in the configurations with the highest expansion velocities when  $N_H \geq 10^{20} [\text{cm}^{-2}]$ .

Finally, Fig. 2 also shows the shift of the median of the profiles for the two outflow geometries. As expected, the median is redder with increasing column density and expansion velocity. The column density has a greater impact than the expansion velocity, since higher values of  $N_H$  imply a larger number of scatterings, thus increasing the reddening of the profiles.

### 3.2 Escape fractions

Fig. 3 compares the predicted Ly $\alpha$  escape fractions in both outflow geometries for a set of column densities, expansion velocities and metallicities, similar to those considered in Fig. 2.

As expected, both outflow geometries predict that the Ly $\alpha$  escape fraction decreases rapidly with increasing  $N_H$ , as the medium becomes optically thicker. High values of the expansion velocity reduce the optical depth of the medium, hence enhancing the Ly $\alpha$  escape fraction.

For the range of properties studied here, we find that the Shell geometry predicts consistently lower Ly $\alpha$  escape fractions than the Wind geometry, for the same set of parameters. This demonstrates that in the detailed interplay of physical conditions shaping  $f_{\text{esc}}$ , the outflow geometry plays an important role.

The difference is less obvious in outflows with  $N_H < 10^{21} [\text{cm}^{-2}]$ , as is the influence of different expansion velocities. At larger column densities, even slightly different expansion velocities can lead to significant differences in the resulting Ly $\alpha$  escape fraction.

Also, in Fig. 3 we show the effect on  $f_{\text{esc}}$  of removing the scattering of photons by hydrogen atoms. We achieve this setting the Ly $\alpha$  scattering cross section to zero as well (i.e.  $H(x) = 0$  in Eq. A4 of Appendix A). The predicted  $f_{\text{esc}}$  is much higher than when considering the scattering by H atoms, and is also independent of expansion velocity, since in our modelling the optical depth of dust depends only on the metallicity and the column density of hydrogen, as shown in Eq. (11). Fig. 3 shows the effect of the resonant scattering resulting from the high cross-section at the line centre increasing the path length, and hence makes the resulting  $f_{\text{esc}}$  lower.

It is interesting to note that even in the case of removing the scatterings by H atoms, the Shell geometry is more sensitive to dust than the Wind geometry, hence showing again the key role of the geometry of the outflows in determining the Ly $\alpha$   $f_{\text{esc}}$ .

## 4 THE MODEL FOR Ly $\alpha$ EMITTERS

In order to understand the nature of the predictions of our model for Ly $\alpha$  emitters, we study in this section the galaxy properties predicted by GALFORM that are relevant in determining the properties of Ly $\alpha$  emitters (Section 4.1), prior to describing how we combine the radiative transfer model for Ly $\alpha$  photons with GALFORM (Section 4.2).

### 4.1 Galaxy properties

Each of our outflow geometries requires a series of galaxy properties, provided by GALFORM, to compute the escape of Ly $\alpha$  photons. We consider the contribution of the disk and the bulge to compute averaged quantities, as described above. These are (i) the half-mass radius,  $R_{1/2}$ , (ii) the circular velocity,  $V_{\text{circ}}$ , (iii) the metallicity of the cold gas,  $Z_{\text{cold}}$ , and (iv) the mass of cold gas of the galaxy,  $M_{\text{gas}}$ . In addition, the Wind geometry requires the mass ejection rate due to supernovae,  $\dot{M}_{\text{ej}}$  (see Eqns. 13 and 17).

Fig. 4 shows the evolution of the galaxy properties listed above in the redshift range  $0 < z < 7$ , as a function of the intrinsic Ly $\alpha$  luminosity,  $L_{\text{Ly}\alpha,0}$ . It is worth noting that these properties are extracted directly from GALFORM, so they do not depend on the details of the outflow model.

In Fig. 4(a) we show the fraction of starbursts as a function of intrinsic Ly $\alpha$  emission. Naturally, given the form of the IMF adopted, starbursts dominate in the brightest luminosity bins, regardless of redshift. However, the transition between quiescent and starburst Ly $\alpha$  emitters shifts towards fainter luminosities as we go to lower redshifts. An important consequence of this trend is that the nature of Ly $\alpha$  emitters, even at a fixed intrinsic Ly $\alpha$  luminosity, is redshift dependent. Moreover, one might expect that the environment in which Ly $\alpha$  photons escape in quiescent galaxies and starbursts is different. Although our fiducial outflow geometries do not make such a distinction, in section 4.2 we make our outflow geometries scale differently with redshift depending on whether galaxies are quiescent or starbursts.

In Fig. 4(b) we show the dependence of the cold gas mass on the intrinsic Ly $\alpha$  luminosity. As expected, in general the cold gas mass increases with  $L_{\text{Ly}\alpha,0}$  at a given redshift, since the latter is directly proportional to the star formation rate of galaxies, and, in this variant of GALFORM, the star formation rate is directly proportional to the cold gas mass, as shown in Eq. (16). Note the star formation timescale is different for quiescent and starburst galaxies (see Baugh et al. 2005 for details on how the star formation is calculated in this variant of GALFORM, and Lagos et al. 2011 for an alternative model).

At low  $L_{\text{Ly}\alpha,0}$  quiescent galaxies dominate, whereas bright galaxies are predominately starbursts. However, there is a luminosity range in which quiescent galaxies and starbursts both contribute. This is shown in Fig. 4(b) by a break in the cold gas mass-luminosity relation, which occurs in the luminosity range where low mass starbursts are as common as massive quiescent galaxies. This luminosity corresponds to  $L_{\text{Ly}\alpha} [\text{erg s}^{-1} \text{ h}^{-2}] \sim 10^{43}$  at  $z \sim 0$ , and it shifts towards fainter Ly $\alpha$  luminosities at higher redshifts. At  $z \sim 6$ , both quiescent and starbursts contribute at  $L_{\text{Ly}\alpha} [\text{erg s}^{-1} \text{ h}^{-2}] \sim 10^{41.5}$ .

The total (disk + bulge) mass ejection rate is found to correlate strongly with the intrinsic Ly $\alpha$  luminosity, as shown in Fig. 4(c). However, no significant evolution is found with redshift. Since the mass ejection rate due to supernovae is directly proportional to the star formation rate, as shown in Eqns. (14) and (15), and the

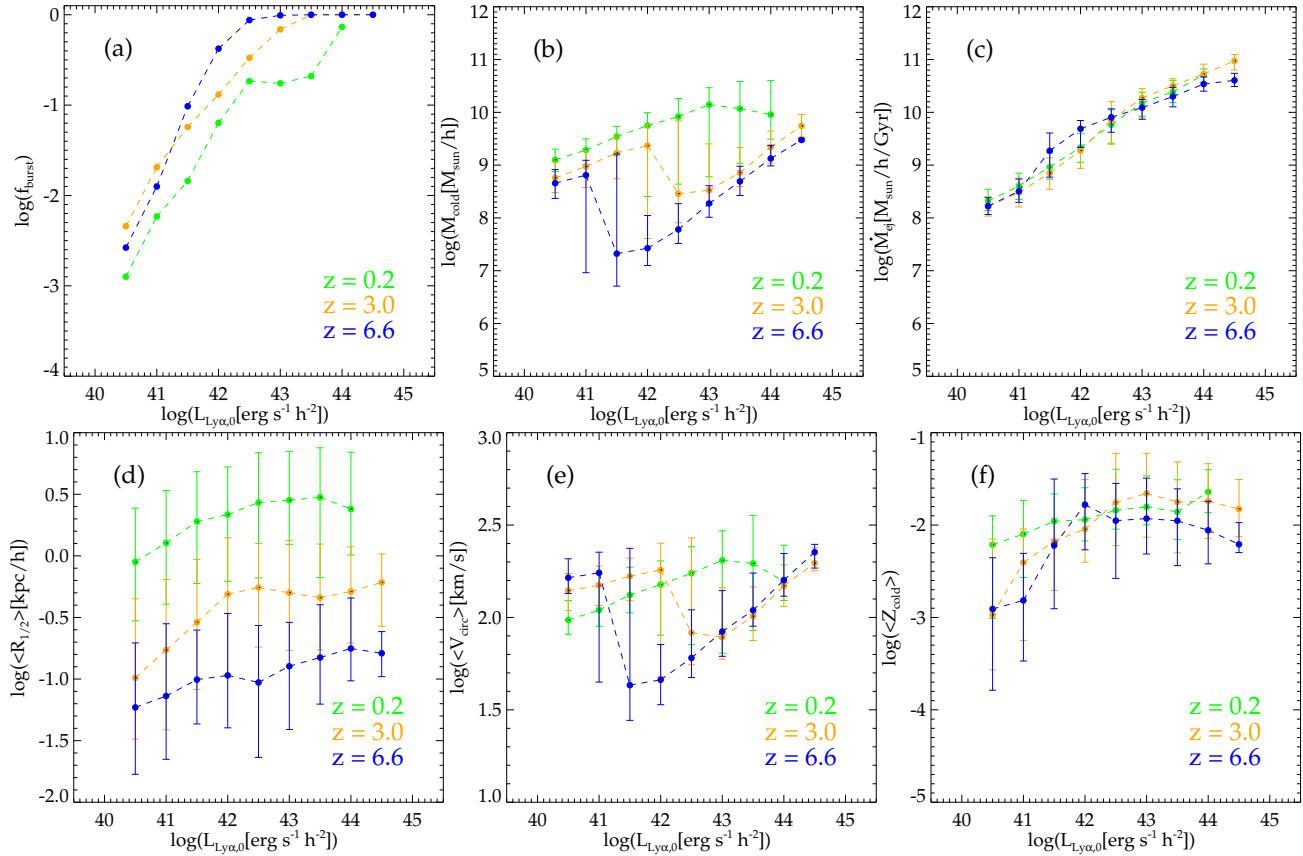


**Figure 4.** The evolution of the galaxy properties predicted by GALFORM which are used as inputs to the outflow geometries for  $z = 0.2$  (green),  $z = 3.0$  (orange) and  $z = 6.6$  (blue). The panels show, as a function of intrinsic  $\text{Ly}\alpha$  luminosity, median values for (a) the fraction of starbursts; (b) the cold gas mass of the galaxy,  $M_{\text{cold}}$ ; (c) the mass ejection rate,  $\dot{M}_{\text{ej}}$ ; (d) the luminosity-weighted half-mass radius,  $\langle R_{1/2} \rangle$ ; (e) the luminosity-weighted circular velocity,  $\langle V_{\text{circ}} \rangle$  and (f) the (mass and  $\text{Ly}\alpha$  luminosity)-weighted metallicity of the gas  $\langle Z_{\text{gas}} \rangle$  (Eq. 9). Error bars show the 10-90 percentile range of the predicted distributions.

conversion between the star formation rate and  $L_{\text{Ly}\alpha,0}$  depends on the production rate of  $\text{Ly}\alpha$  photons, but not on redshift, it is not surprising that the mass ejection rate does not evolve with redshift.

The half-mass radius  $\langle R_{1/2} \rangle$  is the parameter that is found to have the strongest evolution with redshift, as shown in Fig. 4(d). Galaxies at  $z = 0.2$  typically have half-mass radii of a few kpc/h. The median size of galaxies decreases rapidly with increasing redshift, falling by an order of magnitude or more by  $z = 6.6$ . In contrast,  $\langle R_{1/2} \rangle$  varies only weakly with  $L_{\text{Ly}\alpha,0}$ .

The circular velocity of galaxies depends both on their mass and half-mass radius. The sizes of galaxies are computed based on angular momentum conservation, centrifugal equilibrium for disks and virial equilibrium and energy conservation in mergers for spheroids, as described in detail by Cole et al. (2000). We find that the sizes correlate only weakly with the intrinsic  $\text{Ly}\alpha$  luminosity, as shown in Fig. 4(d), and although the total mass of the galaxy is not necessarily related to the cold gas mass, the circular velocity  $\langle V_{\text{circ}} \rangle$  has similar form to the dependence of  $\langle M_{\text{gas}} \rangle$  on  $L_{\text{Ly}\alpha,0}$ , as shown in Fig. 4(e). This explains the break in this relation at  $z = 6.6$ , which corresponds to the switch from quiescent to burst galaxies, as was the case for the cold gas mass.

Finally, the metallicity  $\langle Z_{\text{cold}} \rangle$  correlates strongly with  $L_{\text{Ly}\alpha,0}$  but fairly weakly with redshift, as shown in Fig. 4(f). The metallicity of galaxies with  $L_{\text{Ly}\alpha} [\text{erg s}^{-1} \text{ h}^{-2}] > 10^{42}$  is found to be around  $\sim 10^{-2}$ .

The quantities shown in Fig. 4 are fed into the Monte Carlo

radiative transfer code to calculate the  $\text{Ly}\alpha$  escape fraction  $f_{\text{esc}}$  and the line profile. The net  $\text{Ly}\alpha$  luminosity of the galaxy is then simply  $L_{\text{Ly}\alpha} = f_{\text{esc}} L_{\text{Ly}\alpha,0}$ . The value of  $f_{\text{esc}}$  depends, of course, on the outflow geometry.

## 4.2 Choosing the outflow parameters

In the following, we outline the procedure to choose the value of the free parameters of our outflow models. Our strategy to set the value of these parameters ( $[f_M, f_V, f_R]$  for the Shell geometry, and  $[f_V, f_R]$  for the Wind geometry) consists of matching the observed cumulative  $\text{Ly}\alpha$  luminosity functions (CLFs) in the redshift range  $0 < z < 7$ . Then, we use the values obtained to make the predictions in the remainder of the paper.

A similar strategy was followed in previous modelling of  $\text{Ly}\alpha$  emitters (Le Delliou et al. 2005, 2006; Nagamine et al. 2006; Kobayashi, Totani & Nagashima 2007). However, it is worth pointing out that, to date, the model presented here is the only one that attempts to match the recently observed abundances of  $\text{Ly}\alpha$  emitters at  $z = 0.2$  and at higher redshifts at the same time.

As a first step towards our definitive model, we show in the left panel of Fig. 5 the cumulative luminosity function (CLF) predicted by GALFORM alone and applying a fixed  $f_{\text{esc}}$ , i.e. without using the Monte Carlo radiative transfer code.

The CLF constructed using the intrinsic  $\text{Ly}\alpha$  luminosity of galaxies greatly overpredicts the observed estimates in the redshift

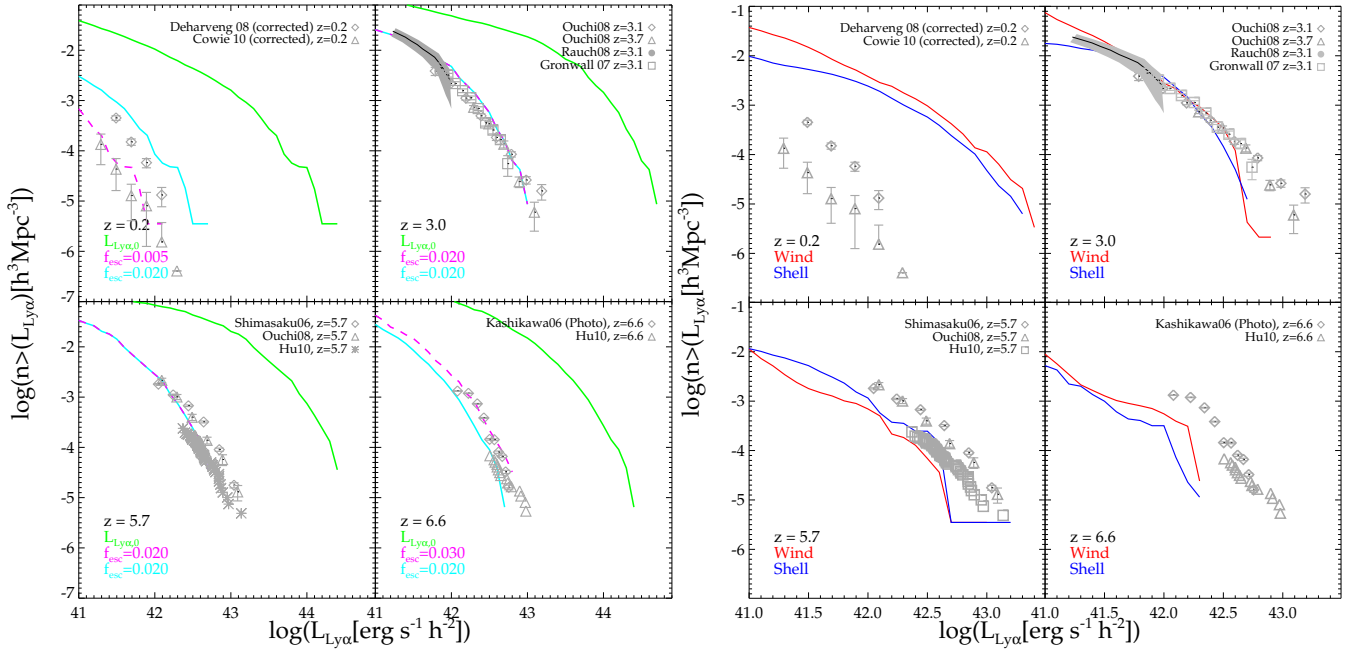


**Figure 5.** The cumulative luminosity function of Ly $\alpha$  emitters at redshifts  $z = 0.2, 3.0, 5.7$  and  $6.6$ . The green lines in the left panel show the CLF obtained using the intrinsic (without attenuation) Ly $\alpha$  luminosity at different redshifts. The cyan lines show the CLF obtained when applying a fixed global escape fraction of  $f_{\text{esc}} = 0.02$  to all galaxies. The magenta dashed lines show the effect of applying an escape fraction that varies with redshift, to match the observational data. The values chosen are written in the labels. The right panel shows with solid red (blue) lines the CLFs obtained with the Wind (Shell) geometry when choosing the free parameters to match the observational CLF at  $z = 3$ , and then the same parameters were then used to predict the CLF at the other redshifts (see the text for details). In both panels, the observational CLFs at each redshift are shown with gray symbols: At  $z = 0.2$  data is taken from Deharveng et al. (2008) and Cowie, Barger & Hu (2010); at  $z = 3.0$  from Gronwall et al. (2007); Ouchi et al. (2008) and Rauch et al. (2008); at  $z = 5.7$  from Shimasaku et al. (2006); Ouchi et al. (2008) and Hu et al. (2010); and at  $z = 6.6$  from Kashikawa et al. (2006) and Hu et al. (2010).

range  $0.2 < z < 6.6$ . This is not surprising, since, as discussed earlier, Ly $\alpha$  photons are expected to suffer an important attenuation due to the presence of dust, and therefore, to have small escape fractions. Fig. 5 shows also the results of the approach followed by Le Delliou et al. (2005, 2006) and Orsi et al. (2008), in which  $f_{\text{esc}} = 0.02$  is adopted for all galaxies, regardless of their physical properties or redshift. This method is equivalent to a global shift in the intrinsic Ly $\alpha$  CLF faintwards. This assumption is able to match remarkably well the observed CLF of Ly $\alpha$  emitters at  $z = 3$ . Also, it is found to provide a good fit to observational estimates at  $z = 5.7$  and to slightly underpredict the observed CLF at  $z = 6.6$ . However, the largest difference occurs at  $z = 0.2$ , where the fixed  $f_{\text{esc}} = 0.02$  scenario overpredicts the observational CLF by a factor of  $\sim 5$  in Ly $\alpha$  luminosity. Note that the  $z = 0.2$  CLF estimate was not available at the time Le Delliou et al. studied Ly $\alpha$  emitters with a constant value for  $f_{\text{esc}}$ , and therefore these authors were not aware of this disagreement.

Fig. 5 also shows the effect of choosing a value for the Ly $\alpha$  escape fraction that varies with redshift. At  $z = 0.2$ , we find that a value of  $f_{\text{esc}} = 0.005$  is needed to match the observational data. At  $z = 6.6$ , a value of  $f_{\text{esc}} = 0.03$  provides a better fit to the observational data than  $f_{\text{esc}} = 0.02$ .

This second method, i.e. varying  $f_{\text{esc}}$  with redshift to find the best fitting value, has been also used in previous works (e.g. Nagamine et al. 2010). Although it reproduces the observed abundances of Ly $\alpha$  emitters at different redshifts, it lacks physical motivation. Therefore, we now turn to implementing our Monte Carlo radiative transfer model to compute  $f_{\text{esc}}$ .

In our implementation of the Ly $\alpha$  radiative transfer code in GALFORM, the code can take anything from a few seconds up to

minutes to run for a single configuration. Hence, the task of finding the best combination of parameters that match the observational CLFs shown in Fig. 5 could be computationally infeasible if we were to run the code on each galaxy from a GALFORM run (which could be in total a few hundred thousand or even millions of galaxies). To tackle this practical issue we construct a grid of configurations for a particular choice of parameters values. This grid spans the values of the physical properties predicted by GALFORM that are relevant to constructing the outflows. The grid is constructed in such way that the number of grid points is significantly smaller (a factor 10 or more) than the number of galaxies used to construct it. An efficient way to construct the grid allows us to run the Monte Carlo radiative transfer code over each of the grid points, hence obtaining a value for  $f_{\text{esc}}$  in a reasonable time. Finally, we interpolate the values of  $f_{\text{esc}}$  in this multidimensional grid for each galaxy in GALFORM, according to their physical parameter values, thus obtaining a value of  $f_{\text{esc}}$  for each galaxy. The methodology to construct the grid and to interpolate the value of  $f_{\text{esc}}$  for each galaxy is described in detail in Appendix C.

Ideally, we would like to find a single set of parameter values to reproduce the observed CLFs at all redshifts. Fig. 5 shows the result of choosing the best combination of parameters to match the observational CLF at  $z = 3$ . We chose this particular redshift because the observational measurements of the CLF at this redshift span a broad range of Ly $\alpha$  luminosities, and the scatter between the different observational estimates of the CLF is smaller than at other redshifts.

For simplicity, we have chosen  $f_V = 1.0$  in both geometries. Also,  $f_M = 0.1$  was used for the Shell geometry. Hence, the only truly adjustable parameter in each model is  $f_R$ . We have found that

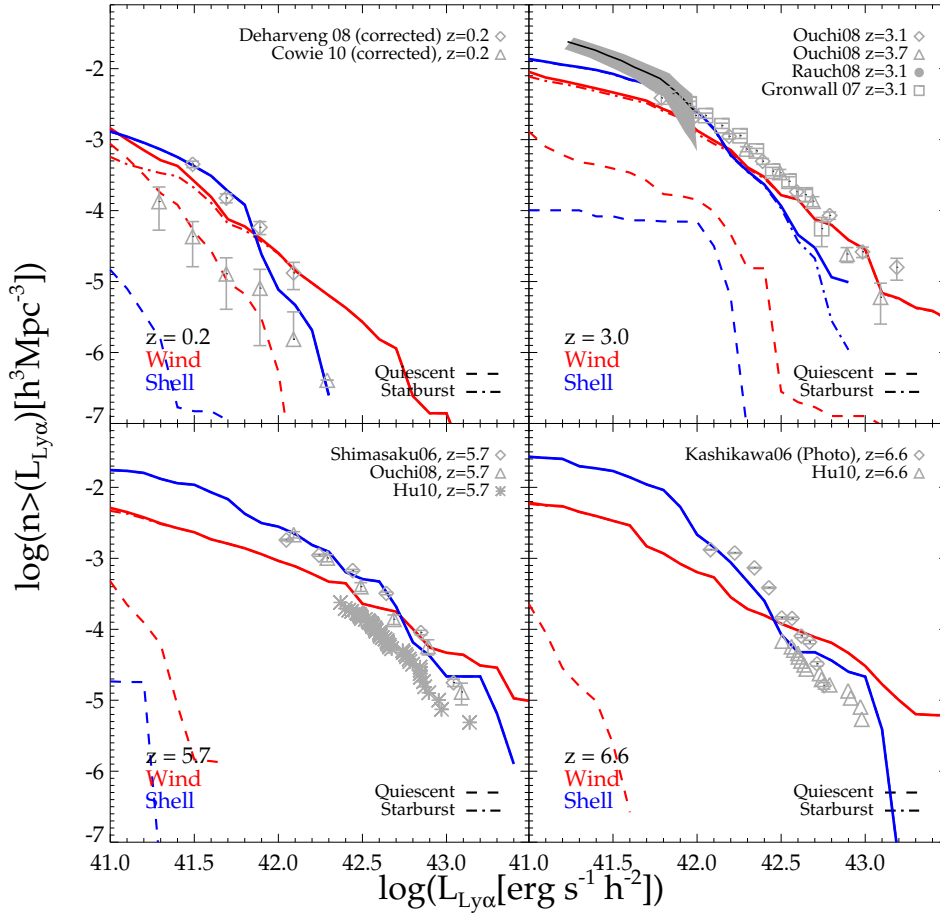


**Figure 6.** The cumulative luminosity function of  $\text{Ly}\alpha$  emitters at redshifts  $z = 0.2, 3.0, 5.7$  and  $6.6$ . The CLF predicted using the Wind geometry is shown with a solid red curve, and the Shell geometry is shown in blue. The contribution of quiescent and starbursts to the model CLFs are shown with dashed and dot-dashed curves, respectively. Note that at  $z \geq 3$  starbursts completely dominate the total CLF. Observational CLFs at each redshift are shown with gray symbols, like in Fig. 5

a value of  $f_R = 0.85$  for the Shell geometry, and  $f_R = 0.15$  for the Wind geometry are needed to match the observed CLF of  $\text{Ly}\alpha$  emitters at  $z = 3$ .

Despite finding a reasonable fit to the observational data at this redshift, neither of our outflow geometries is able to match the observed CLFs over the whole redshift range  $0 < z < 7$  if one fixed set of parameters is used.

As shown in Fig. 5, the observed CLF at  $z = 0.2$  is particularly difficult to match when the model parameters have been set to match the CLFs at higher redshift. This occurs because the number density of  $\text{Ly}\alpha$  emitters at  $z = 0.2$  reported observationally (Deharveng et al. 2008; Cowie, Barger & Hu 2010) is much lower than what our model predicts, implying  $f_{\text{esc}}$  is also considerably lower than what our model suggests. On the other hand, the observed CLF at  $z = 6.6$  implies a higher abundance of  $\text{Ly}\alpha$  emitters than what our model for computing the  $\text{Ly}\alpha$  escape fraction predicts.

An improved strategy to reproduce the observed CLFs of  $\text{Ly}\alpha$  emitters at  $0 < z < 7$  is to choose the free parameters of the models in the following way:

(i) The expansion velocity of the outflows is set to be equal to the  $\text{Ly}\alpha$ -weighted circular velocity of the galaxies (i.e.  $f_V = 1$  in both geometries).

(ii) In the Shell geometry, the fraction of cold gas mass in the outflow is fixed at  $f_M = 0.1$ .

(iii) Given the strong evolution of the half-mass radius of galaxies with redshift, the value of  $f_R$  is allowed to evolve with redshift.

Galaxies at low redshift are predicted to be larger in size than galaxies at higher redshifts, so if  $f_R$  is fixed like the other parameters, then outflows at lower redshift would have, on average, larger sizes than at high redshifts, making the associated column densities smaller (see Eqs. 1 and 19). If the other outflow properties do not evolve strongly with redshift, then galaxies at low redshift would have larger  $\text{Ly}\alpha$  escape fractions than at higher redshifts. As discussed above, this is the opposite trend needed to reproduce the observed CLFs.

However, there is growing evidence that star forming regions in local ultraluminous infrared galaxies (ULIRGS) are significantly smaller than similarly luminous ULIRGS and submillimetre galaxies (SMGs) at higher redshifts (see Iono et al. 2009; Rujopakarn et al. 2011, for a comparison of sizes). If the outflow radius in starbursts is assumed to scale with the size of the star forming regions instead of the full galaxy size, then  $f_R$  would have a natural redshift dependence in the direction we need.

Hence, we employ a simple phenomenological evolution of  $f_R$  with redshift. We call  $f_R^b$  the radius parameter of starbursts and

	$f_M$	$f_V$	$f_R^q$	$f_{R,0}^b$	$\gamma$
Shell	0.10	1.00	0.200	0.223	0.925
Wind	–	1.00	0.015	0.014	2.152

**Table 1.** Summary of the parameter values of the Shell and Wind geometries used to fit the Ly $\alpha$  cumulative luminosity function at different redshifts (see the text for details).

allow it to scale with redshift like a power-law:

$$f_R^b = f_{R,0}^b (1+z)^\gamma, \quad (21)$$

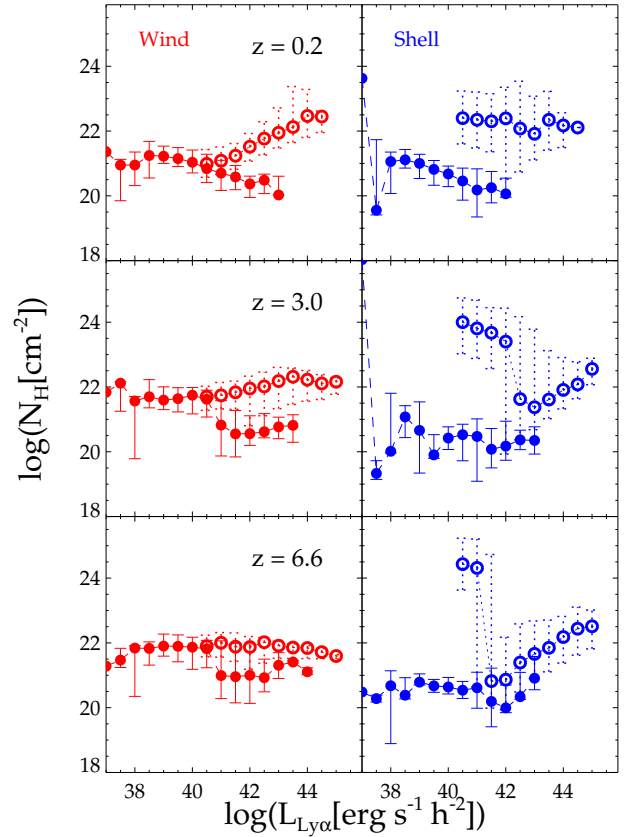
where  $f_{R,0}^b$  and  $\gamma$  are free parameters. Since there is no equivalent observational evidence for the size of star forming regions in quiescent galaxies scaling with redshift, we set  $f_R^q$ , the radius parameter for quiescent galaxies, to be an adjustable parameter but fixed (i.e. independent of redshift).

Table 1 summarizes a suitable choice of the parameters values used in our model. Also, Fig. 6 shows the predicted cumulative luminosity functions obtained with that choice of parameters.

Our previous modelling of Ly $\alpha$  emitters used the simple assumption of a constant Ly $\alpha$  escape fraction, with  $f_{\text{esc}} = 0.02$  being a suitable value to reproduce the Ly $\alpha$  CLFs at  $3 < z < 7$  (Le Delliou et al. 2005, 2006; Orsi et al. 2008). As shown in Fig. 5, this simple model overestimates the CLF at  $z = 0.2$ , but it reproduces remarkably well the CLFs at higher redshifts. Our outflow geometries, on the other hand, are consistent with the observational CLFs at all redshifts, although they fail to reproduce their full shape. This may be surprising at first, since the intrinsic Ly $\alpha$  CLF (shown in green in Fig. 5) roughly reproduces the shape of the observed CLFs, although displaced to brighter luminosities (which is why the constant escape fraction scenario works well at reproducing the CLFs). However, in our model, the escape fraction in each galaxy is the result of a complex interplay between several physical properties, and this in turn modifies the resulting shape of the CLF.

The sizes of the outflows predicted by our model, compared to the extent of the galaxies themselves (quantified by the half-mass radius  $\langle R_{1/2} \rangle$ ) are very different between the two outflow geometries. In quiescent galaxies these are 1.5 and 20 percent of the half-mass radius of the galaxies, in the Wind and Shell geometries respectively. Similarly, at  $z = 0.2$ , outflows in starbursts are 2 and 26 percent of the half-mass radius in the Wind and Shell geometries. The rather small size of outflows in the Wind geometry appears to be in contradiction with observations of Ly $\alpha$  in local starbursts which display galactic-scale outflows (see, e.g. Giavalisco, Koratkar & Calzetti 1996; Thuan & Izotov 1997; Kunth et al. 1998; Mas-Hesse et al. 2003; Östlin et al. 2009; Mas-Hesse et al. 2009). However, local starburst samples are sparse and still probably not large enough to characterise the nature (in a statistical sense) of Ly $\alpha$  emitters at low redshifts.

At higher redshifts, our model keeps the sizes of outflows in quiescent galaxies unchanged (with respect to their half-mass radius). However, outflows in starbursts grow in radius, relative to their host galaxy, according to a power law, as given by Eq. (21), with the best fitting values listed in Table 1, so at  $z = 3$  their sizes are 27 and 80 percent of the half-mass radius for the Wind and Shell geometries, respectively. By  $z = 6.6$ , the sizes are 110 and 145 percent of the half-mass radius. Therefore, at  $z \gtrsim 3$ , all outflows in Ly $\alpha$ -emitting starbursts are galactic-scale according to our models.



**Figure 7.** The neutral hydrogen column density of outflows for galaxies as a function of Ly $\alpha$  luminosity at redshifts  $z = 0.2$  (top),  $z = 3.0$  (middle) and  $z = 6.6$  (bottom). The Wind geometry is shown in red (left), and the Shell geometry in blue (right). Filled circles show the median of the column density distribution as a function of the attenuated Ly $\alpha$  luminosity. Open circles show the same but as a function of the intrinsic Ly $\alpha$  luminosity. Error bars show the 10-90 percentiles of the column density distribution at each Ly $\alpha$  luminosity bin.

A consequence of setting the free parameters in the model to reproduce the low- $z$  data is that the CLF of Ly $\alpha$  emitters at  $z = 0.2$  has a contribution from both quiescent and starburst galaxies. Despite the details over which component is dominant at this redshift (which is something somewhat arbitrary given the freedom to adjust the other free parameters of the models), the CLF of Ly $\alpha$  emitters at high redshifts is invariably dominated by starbursts, and only a negligible fraction of Ly $\alpha$  emitters are quiescent galaxies.

## 5 PROPERTIES OF Ly $\alpha$ EMISSION

Having chosen the parameters in our outflow geometries we proceed to study the predictions of our hybrid model for the properties of Ly $\alpha$  emitters. Whenever possible, we compare our predictions with available observational data.

### 5.1 Column densities

An immediate consequence of the choice of parameters shown in Table 1 is the distribution of predicted column densities of the outflows of galaxies. The derived hydrogen column density is shown in Fig. 7, as a function of Ly $\alpha$  luminosity for different redshifts.



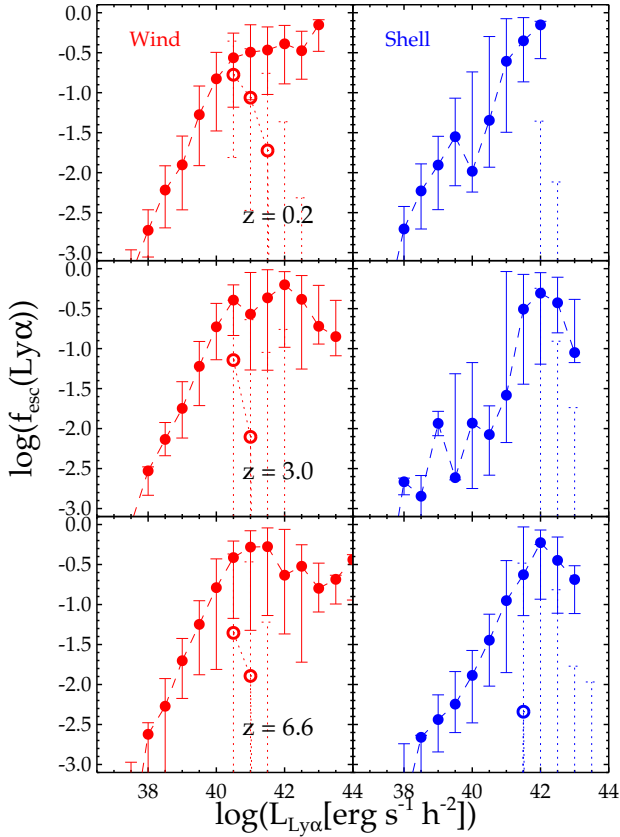


**Figure 8.** The escape fraction as a function of Ly $\alpha$  luminosity at  $z = 0.2$  (top),  $z = 3.0$  (middle) and  $z = 6.6$  (bottom). The Wind geometry predictions are shown in red (left), and the Shell geometry in blue (right). Solid circles show the median of the escape fraction at different attenuated Ly $\alpha$  luminosity bins. Open circles show the same relation as a function of intrinsic Ly $\alpha$  luminosity instead. Error bars represent the 10-90 percentiles around the median of the escape fraction distribution at a given Ly $\alpha$  luminosity bin.

Here we study this distribution both as a function of intrinsic and attenuated Ly $\alpha$  luminosity.

When studied as a function of intrinsic Ly $\alpha$  luminosity, our model displays a large range of column densities, varying from  $N_H \sim 10^{21} [\text{cm}^{-2}]$  to  $N_H \sim 10^{24} [\text{cm}^{-2}]$ , depending on the outflow geometry and the redshift. Typically, in both outflow geometries, the column density increases with intrinsic Ly $\alpha$  luminosity, which is due to the overall increase in the mass of cold gas and the mass ejection rate with intrinsic Ly $\alpha$  luminosity. However, in some cases, there is a noticeable decrease of the column density with increasing intrinsic Ly $\alpha$  luminosity, reflecting the rather complicated relation between the quantities which affect the column density and the intrinsic Ly $\alpha$  luminosity, as shown in Fig. 4.

When including attenuation due to dust, this relation is modified, as shown by the solid circles in Fig. 7. The number of scatterings scales with the column density of the medium, hence the escape fraction is low (or effectively zero in some cases, according to our model) for outflows with large column densities. As a result, the column density distribution as a function of attenuated Ly $\alpha$  luminosity spans  $N_H \sim 10^{19-22} [\text{cm}^{-2}]$ . Also, galaxies with brighter (attenuated) Ly $\alpha$  luminosities tend to have smaller column densities.

The column densities predicted by our models are similar to those inferred by Verhamme et al. (2008) on fitting their models to

a small sample of high redshift galaxies with high resolution spectra. These authors fit Ly $\alpha$  line profiles with a Monte Carlo radiative transfer model using a geometry identical to our Shell geometry. In addition, Verhamme et al. present a compilation of results for observationally-measured column densities of local starbursts showing Ly $\alpha$  emission, with values between  $10^{19} - 10^{22} [\text{cm}^{-2}]$ , which are also consistent with our model predictions.

## 5.2 Ly $\alpha$ escape fractions

A fundamental prediction of our models is the distribution of Ly $\alpha$  escape fractions, shown in Fig. 8. In terms of the attenuated Ly $\alpha$  emission, we find that  $f_{\text{esc}}$  grows monotonically from  $10^{-3}$  in the faintest Ly $\alpha$  emitters (with  $L_{\text{Ly}\alpha} \sim 10^{38} [\text{erg s}^{-1} \text{h}^{-2}]$ ) to  $f_{\text{esc}} \sim 0.3$  at  $L_{\text{Ly}\alpha} \sim 10^{40} [\text{erg s}^{-1} \text{h}^{-2}]$ . Brighter galaxies have in general escape fractions ranging from 0.1 to  $\sim 1$ , depending on the redshift and outflow geometry. Perhaps not surprisingly, both models predict similar distributions of escape fractions as a function of Ly $\alpha$  luminosity, since the models are forced to match the observed CLFs (Section 4.2).

On the other hand, in terms of the intrinsic Ly $\alpha$  emission, Fig. 8 shows that only in some cases it is possible to obtain a median  $f_{\text{esc}}$  above zero. This reflects the complicated interplay of physical conditions which shape the escape fraction of Ly $\alpha$  photons. In other words, the value of the intrinsic Ly $\alpha$  luminosity in a galaxy does not determine  $f_{\text{esc}}$  and, therefore, its attenuated Ly $\alpha$  luminosity.

Fig. 8 illustrates further the contrast between using a physical model to compute the Ly $\alpha$  escape fraction, and the constant  $f_{\text{esc}}$  scenario. In the former, galaxies seen with high Ly $\alpha$  luminosities have high escape fractions, so their intrinsic Ly $\alpha$  luminosities are similar to the attenuated ones. Fainter galaxies, on the other hand, have lower escape fractions, meaning that their intrinsic Ly $\alpha$  luminosity is orders of magnitude higher than their observed luminosity. This implies that a Ly $\alpha$  emitter with a given intrinsic Ly $\alpha$  luminosity could have either a high or low value of  $f_{\text{esc}}$ , depending on its physical characteristics (galaxy size, metallicity, circular velocity, SFR, etc.). In the constant escape fraction scenario, on the other hand, all galaxies at a given observed Ly $\alpha$  luminosity have the same intrinsic luminosity, which means that galaxies need only to have a high intrinsic Ly $\alpha$  luminosity to be observed as Ly $\alpha$  emitters.

We conclude from Fig. 8 that a high production of Ly $\alpha$  photons (or, equivalently, high intrinsic Lyman continuum luminosity) does not guarantee that a galaxy is visible in Ly $\alpha$ . Our modelling of the escape fraction selects a particular population of galaxies to be observed as Ly $\alpha$  emitters, which in general is found to have lower metallicities, lower SFRs and larger half-mass radii than the bulk of the galaxy population. This is discussed in more detail in Section 6.

It is worth asking at this point whether the predicted escape fractions are consistent with observational estimates. Observationally,  $f_{\text{esc}}$  is generally calculated either by inferring the SFRs from the Ly $\alpha$  luminosity and comparing to the SFR estimated from the UV continuum (e.g. Gawiser et al. 2006; Blanc et al. 2011; Guaita et al. 2010), or by using the ratio between Ly $\alpha$  and another non-resonant hydrogen recombination line. The former requires assumptions about the stellar evolution model, the choice of the IMF and the modelling of dust extinction. The second method only relies on the assumption that the comparison line is not affected by resonant scattering, and thus the extinction can be estimated reliably from an extinction curve, and that the intrinsic line ratio cor-

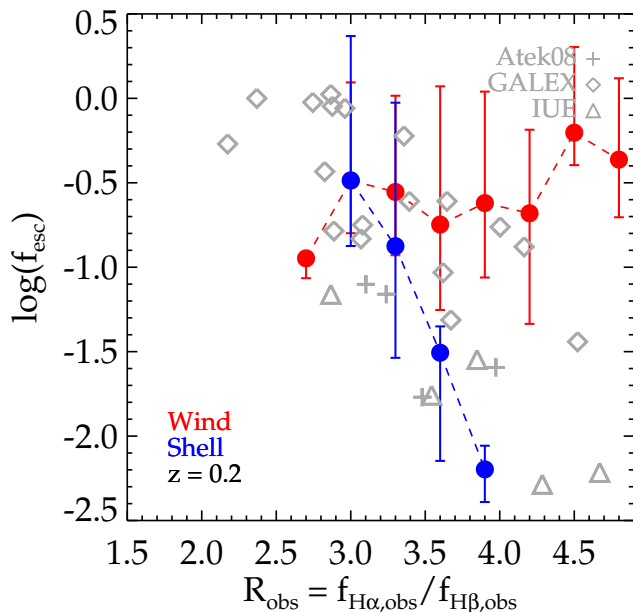


**Figure 9.** The Ly $\alpha$  escape fraction as a function of the observed (i.e. attenuated) ratio of H $\alpha$  to H $\beta$  flux at  $z = 0.2$ . Red circles show the median predictions using the Wind geometry, and blue circles show the median predictions of the Shell geometry. Error bars in both cases show the 10-90 percentiles of the distribution. Grey symbols show observational measurements by Atek et al. (2008) (crosses), and GALEX and IUE samples (diamonds and triangles respectively) from Atek et al. (2009).

responds to the ratio of the emission coefficients, assuming case B recombination.

For this reason, we focus on the escape fraction measured using line ratios. These are often presented as a function of colour excess  $E(B - V)$ , which in turn is estimated from non-resonant recombination lines such as H $\alpha$  and H $\beta$  together with an assumed extinction curve, which describes foreground extinction (Atek et al. 2008, 2009; Östlin et al. 2009; Hayes et al. 2010). For the purposes of comparing the model predictions to the observationally-estimated values of  $f_{\text{esc}}$ , we convert the values of  $E(B - V)$  quoted in the observations to  $R_{\text{obs}} \equiv f_{\text{H}\alpha, \text{obs}} / f_{\text{H}\beta, \text{obs}}$ , the ratio between the observed fluxes of H $\alpha$  and H $\beta$ , since this ratio is a direct prediction from GALFORM. To compute  $R_{\text{obs}}$ , we follow a standard relation (Atek et al. 2008),

$$\log(R_{\text{obs}}) = \log(R_{\text{int}}) - E(B - V) \frac{k(\lambda_{\alpha}) - k(\lambda_{\beta})}{2.5}, \quad (22)$$

where  $R_{\text{int}} = 2.86$  is the intrinsic line ratio between H $\alpha$  and H $\beta$  typically assumed under Case B recombination for a medium at a temperature of  $T = 10000\text{K}$  (Osterbrock 1989), and  $k(\lambda_{\alpha}) = 2.63$ , and  $k(\lambda_{\beta}) = 3.71$  are the values of the normalized extinction curve at each corresponding wavelength from the extinction curve of Cardelli, Clayton & Mathis (1989).

Fig. 9 shows the predicted relation between the Ly $\alpha$  escape fraction and  $R_{\text{obs}}$  compared to observational estimates from Atek et al. (2008) and an analysis of UV spectroscopic data from the GALEX and IUE surveys by Atek et al. (2009).

The model predictions shown in Fig. 9 include only galaxies with  $\log(L_{\text{Ly}\alpha} [\text{erg s}^{-1} \text{h}^{-2}]) > 41.5$ , in order to approximately reproduce the selection of Ly $\alpha$  emitters in the GALEX sample. Note, however, that the observational points shown in Fig. 9 do not represent a complete statistical sample. Therefore it is not possible

to perform a fair comparison, and the results shown here should be regarded as illustrative.

The Shell geometry shows remarkable agreement with the observational estimates of  $f_{\text{esc}}$ , reproducing the trend of lower escape fractions in galaxies with larger  $R_{\text{obs}}$ . The Wind geometry, on the other hand, is only partially consistent with the observational data, and it predicts a rather flat relation between  $f_{\text{esc}}$  and  $R_{\text{obs}}$ .

### 5.3 The Ly $\alpha$ Equivalent width distribution

The equivalent width  $EW$  measures the strength of the line with respect to the continuum around it. We compute the  $EW$  simply by taking the ratio of the predicted Ly $\alpha$  luminosity of galaxies and the stellar continuum around the Ly $\alpha$  line as computed by GALFORM, including attenuation by dust. Fig. 10 shows a comparison of the  $EW$  distribution measured at different redshifts with the predictions from our outflow geometries.

Overall, both outflow geometries predict  $EW$  distributions broader than the observational samples for all redshifts studied. To characterise the predicted  $EW$ s, we compute the median of the distributions. This will depend on the Ly $\alpha$  luminosity limit applied to the sample to make a fair comparison with observed data. In Fig. 10 we compare our model predictions with observational data from Cowie, Barger & Hu (2010) at  $z = 0.2$ , Ouchi et al. (2008) at  $z = 3.1$  and also at  $z = 5.7$ .

The comparison between the observed and predicted  $EW$  by the Wind geometry median values (shown by vertical dashed lines in the left panel of Fig. 10) is encouraging at  $z = 0.2$ , where the  $EW$  distributions have a median value of  $\sim 30 \text{ \AA}$ . However, both geometries give consistently higher median values of the  $EW$  when compared to the observational data at higher redshift. In addition, the disagreement in the median values of the  $EW$  distribution between observational data and the Shell geometry predictions becomes larger as we go to higher redshifts.

At  $z = 0.2$ , the  $EW$  distribution predicted using both outflow geometries is broader than the observational sample of Cowie, Barger & Hu (2010) and reaches values of  $EW \approx 300 \text{ \AA}$ , whereas the observational sample only reaches  $EW \approx 130 \text{ \AA}$ .

At  $z = 3.0$ , the observational sample seems to peak around an  $EW \approx 80 \text{ \AA}$  and then declines until reaching  $EW \approx 150 \text{ \AA}$ . The predicted  $EW$ s are consistent with the observational distributions, although the former reach values as high as  $EW \approx 400 \text{ \AA}$ . A similar disagreement between model predictions and observational data is found at  $z = 5.7$ .

The disagreement found between the  $EW$  values in the model predictions and the observations is difficult to understand from studying only the  $EW$  distributions. Therefore, we perform a more detailed comparison by studying the relation between the median  $EW$  and the Ly $\alpha$  luminosity, as shown in the right panels of Fig. 10.

Fig. 10 shows that there is good agreement between the model predictions and the observational data at  $z = 0.2$ , where both models seem to reproduce the range and scatter of the observations. Overall, both models predict an increase of  $EW$  towards brighter Ly $\alpha$  emitters: The Wind geometry predicts that the median  $EW$  increases from  $\approx 30 \text{ \AA}$  to  $\approx 100 \text{ \AA}$  for Ly $\alpha$  luminosities  $L_{\text{Ly}\alpha} \approx 10^{40} - 10^{42} [\text{erg s}^{-1} \text{h}^{-2}]$ , whereas the Shell geometry predicts a much steeper increase of the median  $EW$ s, from  $\approx 3 \text{ \AA}$  to  $\approx 100 \text{ \AA}$  over the same Ly $\alpha$  luminosity range.

At  $z = 3$ , the  $EW$  values from the observed data are also consistent with both model predictions. The Shell geometry predicts a steep increase in the  $EW$  values with increasing Ly $\alpha$  luminosity,



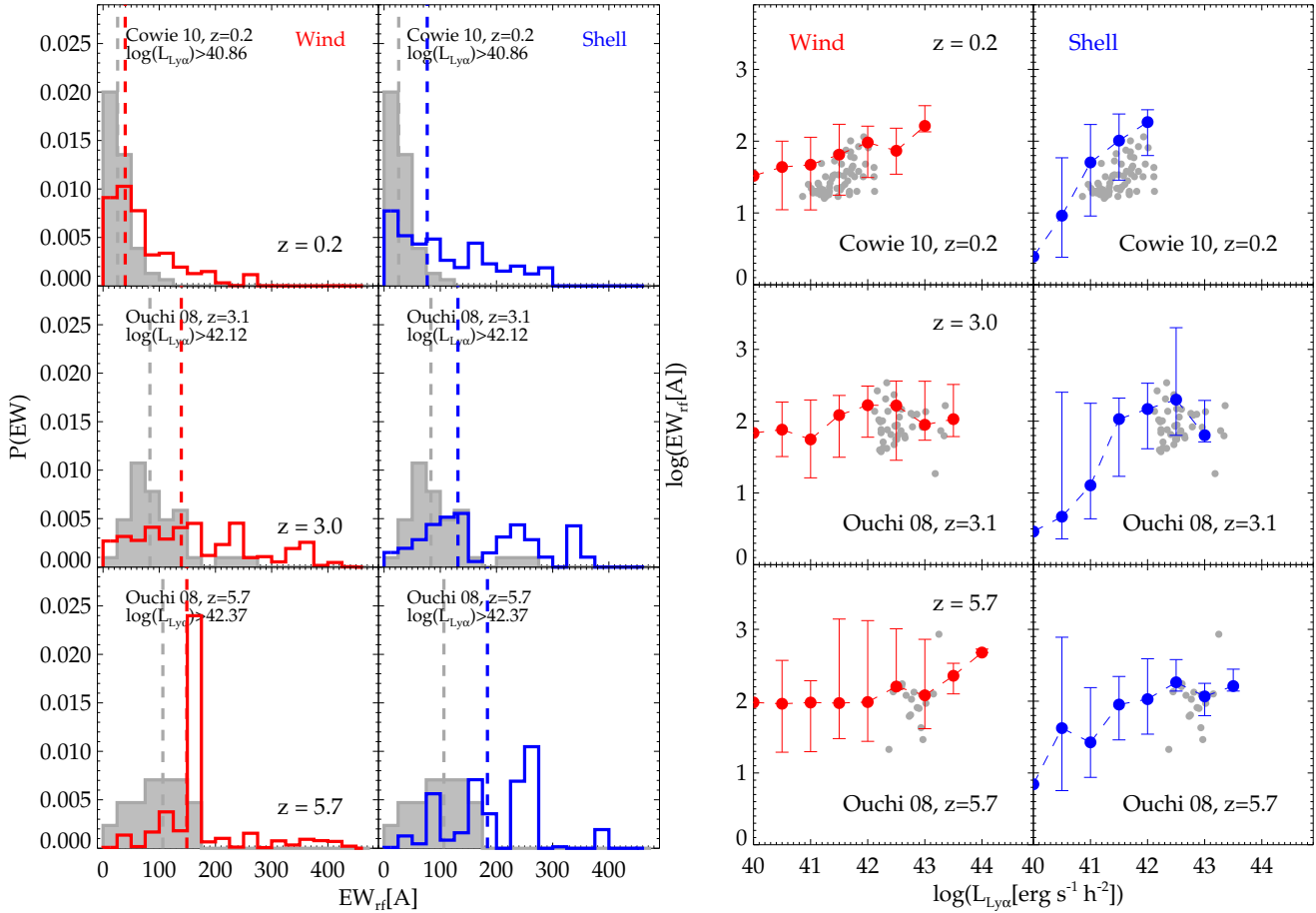


**Figure 10.** The (rest-frame) equivalent width distribution at  $z = 0.2$ ,  $3.0$  and  $z = 5.7$ . The left panels show histograms of the distribution of EWs at different redshifts with the applied lower luminosity limit given in the boxes. The right panels show the median of the distribution of EWs as a function of  $\text{Ly}\alpha$  luminosity. In all cases, the Wind geometry predictions are shown in the left column in red, and the Shell geometry in the right column in blue. The error bars on the right panel denote the 10-90 percentiles of the distribution of EWs. Observational data (shown in gray) is taken from Cowie, Barger & Hu (2010) at  $z = 0.2$  and Ouchi et al. (2008) for redshifts  $z = 3$  and  $z = 5.7$ . The vertical dashed lines in the left panel correspond to the median values of the distributions.

whereas the Wind geometry shows a rather flat relation. At  $z = 5.7$  the models are also consistent with most of the observed EW values within the predicted range of the EW distributions.

#### 5.4 UV continuum properties of $\text{Ly}\alpha$ emitters

The variant of GALFORM used in this work has been previously shown to match the abundance of LBGs (characterised by their UV luminosities) over a wide range of redshifts (Baugh et al. 2005; Lacey et al. 2011; Gonzalez et al. 2011). Therefore, a natural prediction to study with our model is the UV LF of a  $\text{Ly}\alpha$ -selected sample.

Fig. 11 shows the UV (1500 Å) LF of  $\text{Ly}\alpha$  emitters at redshifts 3.0, 5.7 and 6.6. To compare the model predictions with observational data, we mimic the UV selection applied to each sample. These correspond to constraints on the limiting  $\text{Ly}\alpha$  luminosity and the minimum EW. Moreover, we have chosen to compare our model predictions with two observational samples at each redshift. Although the observational samples show similar limiting  $\text{Ly}\alpha$  luminosity at each redshift, the value of the minimum EW, which is different among observational samples, has an important impact on the predicted UV LF of  $\text{Ly}\alpha$  emitters, as shown in Fig. 11.

At  $z = 3$ , we compare our model predictions with the UV

LF from Ouchi et al. (2008) and Gronwall et al. (2007). Overall, our models are found to underpredict the observational estimates, although they are consistent with the faint end of the LF measured by Gronwall et al. (2007), and in reasonable agreement at the bright end with the observational sample of Ouchi et al. (2008). Likewise, at  $z = 5.7$  both outflow geometries are found to underpredict the UV LF of  $\text{Ly}\alpha$  emitters measured by Shimasaku et al. (2006) and Ouchi et al. (2008).

The situation is somewhat different at  $z = 6.6$ . Both outflow geometries are consistent with the faint end of the UV LF of  $\text{Ly}\alpha$  emitters shown in Kobayashi, Totani & Nagashima (2010), who recalculated the UV LF of  $\text{Ly}\alpha$  emitters from the sample of Kashikawa et al. (2006) after applying a brighter  $\text{Ly}\alpha$  luminosity cut, to ensure that a more complete sample was analysed. Also, both outflow geometries are consistent with the UV LF of  $\text{Ly}\alpha$  emitters measured by Cowie, Hu & Songaila (2011).

For comparison, we show in Fig. 11 the UV LF of all galaxies predicted by GALFORM, i.e. without applying any selection. Note this was already shown to agree remarkably well with observed LFs of LBGs in Lacey et al. (2011). This *total* UV LF is always above the UV LF of  $\text{Ly}\alpha$  emitters predicted by the outflow geometries.

At  $z = 3$ , we notice that the UV LF of all galaxies is above the observed LFs of  $\text{Ly}\alpha$  emitters. This is consistent with the idea

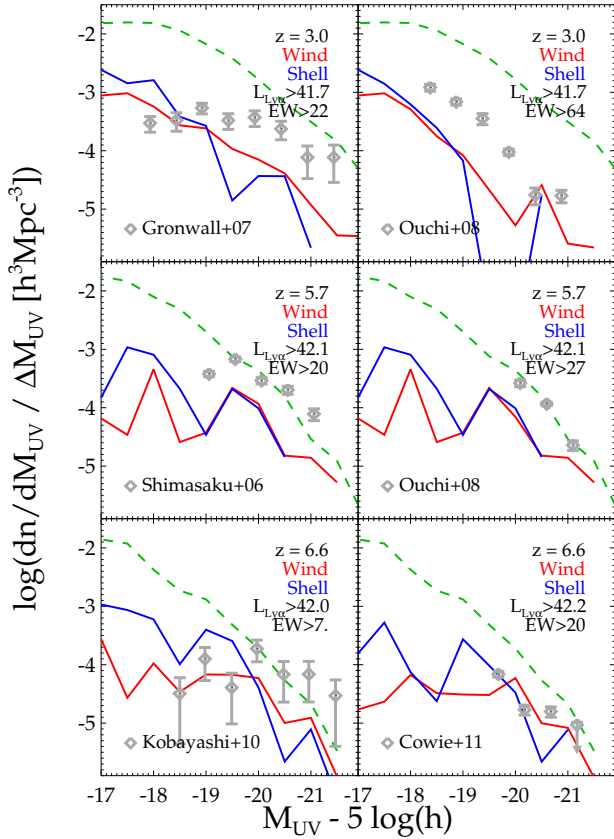


**Figure 11.** The UV luminosity function of Ly $\alpha$  emitters at redshifts  $z = 3.0$  (top),  $z = 5.7$  (middle) and  $z = 6.6$  (bottom). The Wind geometry predictions are shown in red, and those of the Shell geometry in blue. Observational data, shown with gray symbols, is taken from Ouchi et al. (2008) and Gronwall et al. (2007) at  $z = 3$ , Shimasaku et al. (2006) and Ouchi et al. (2008) at  $z = 5.7$  and Kobayashi, Totani & Nagashima (2010) at  $z = 6.6$ . The limiting Ly $\alpha$  luminosity and EW used to construct the models UV LF are shown in each panel, in units of  $\log([\text{erg s}^{-1} \text{ h}^{-2}])$  and  $[\text{\AA}]$ , respectively. The dashed green curves show the UV LF of all galaxies, as predicted by GALFORM, without imposing any Ly $\alpha$  selection.

that Ly $\alpha$  emitters constitute a sub-sample of the galaxy population. However, at  $z = 5.7$  and  $z = 6.6$  this UV LF matches remarkably well the observed UV LFs of Ly $\alpha$  emitters. A similar finding has also been reported in observational papers (e.g. Kashikawa et al. 2006; Ouchi et al. 2008) when comparing the UV LF of LBGs to that of Ly $\alpha$  emitters. Interestingly, only the observational LF from Cowie, Hu & Songaila (2011) falls significantly below the predicted total UV LF of all galaxies, and is at the same time consistent with the predicted UV LF of Ly $\alpha$  emitters for both outflow geometries.

It has been argued that attenuation by the IGM might play a significant role in shaping the LF of Ly $\alpha$  emitters at  $z > 5$ . Kashikawa et al. (2006) interpret their measured LF of Ly $\alpha$  emitters as evidence of an abrupt decrease in the amplitude of the bright end of the Ly $\alpha$  LF at  $z = 6.6$  compared to  $z = 5.7$ . Since the corresponding UV LFs of Ly $\alpha$  samples do not seem to evolve in the same way, this has been suggested as a result of a change in the ionization state of the IGM (for which Ly $\alpha$  photons are more sensitive than continuum photons).

Our model does not compute any attenuation by the IGM. The effect of reionization in GALFORM is modeled simply by preventing the cooling of gas in haloes of a given circular velocity ( $V_{\text{circ}} =$

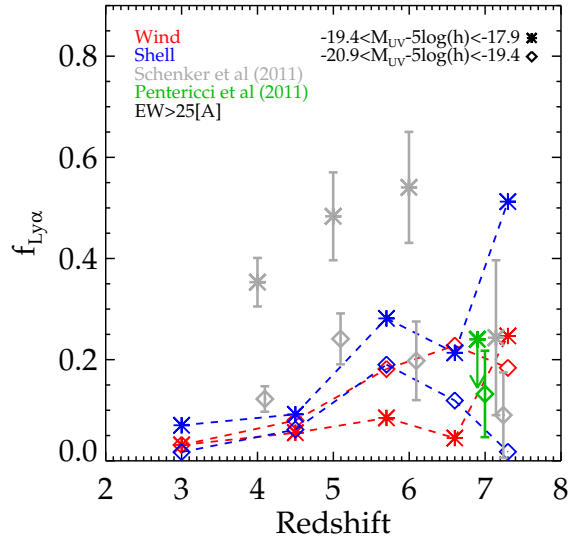


**Figure 12.** The fraction of Ly $\alpha$  emitters with rest-frame equivalent width  $EW_{\text{rf}} > 25 \text{\AA}$  for galaxies with  $-19.4 < M_{\text{UV}} - 5 \log(h) < -17.9$  (asterisks) and  $-20.9 < M_{\text{UV}} - 5 \log(h) < -19.4$  (diamonds) as a function of redshift. Predictions of the Wind and Shell geometries are shown in red and blue, respectively. The observational measurements of Schenker et al. (2011) and Pentericci et al. (2011) are shown in gray and green, respectively.

30 km/s in our GALFORM variant), when their redshift is smaller than a redshift  $z_{\text{reion}} = 10$  (see Benson et al. 2002, for a more detailed model).

Some theoretical work exploring the abundances of Ly $\alpha$  emitters at these high redshifts has attempted to take into account the attenuation of the Ly $\alpha$  line due to absorption by the IGM (Kobayashi, Totani & Nagashima 2007; Dayal, Maselli & Ferrara 2011; Kobayashi, Totani & Nagashima 2010). In our model, a simple mechanism to improve the agreement between the observed and predicted UV LFs of Ly $\alpha$  emitters at high redshift would be to add a constant attenuation factor of the Ly $\alpha$  luminosity by the IGM at high redshifts, set to match the UV LF of Ly $\alpha$  emitters. We defer doing this to a future paper.

We now focus on the fraction of galaxies exhibiting Ly $\alpha$  in emission predicted by our models. As described in Appendix C, in our radiative transfer model we follow a maximum of 1000 photons per galaxy, and so we can compute a minimum value for the escape fraction of  $10^{-3}$ . However, in a significant fraction of galaxies, none of the photons escape from the outflows, resulting in them being assigned  $f_{\text{esc}} = 0$ , and thus having no Ly $\alpha$  emission at all. These galaxies could be related to the observed population of galaxies showing Ly $\alpha$  in absorption (e.g. Shapley et al. 2003), which we will examine in a future paper.

Fig. 12 compares our model predictions with the observed fraction of Ly $\alpha$  emitters found in Lyman-break galaxies (LBGs) at  $z \sim 4 - 7$  by Schenker et al. (2011) and by Pentericci et al. (2011) at  $z \sim 7$ . Ly $\alpha$  emitters are defined here as galaxies with a Ly $\alpha$   $EW_{\text{rf}} \geq 25 \text{\AA}$ . The samples are split according to two different rest-frame UV magnitudes ranges, as shown in Fig. 12. For simplicity, we define UV magnitudes at rest-frame 1500  $\text{\AA}$ .

For the two ranges of UV-magnitudes shown, the Shell geometry appears to have a larger fraction of Ly $\alpha$  emitters as a function of redshift than the Wind geometry. When comparing to the observational data of Schenker et al. (2011), we find that overall both

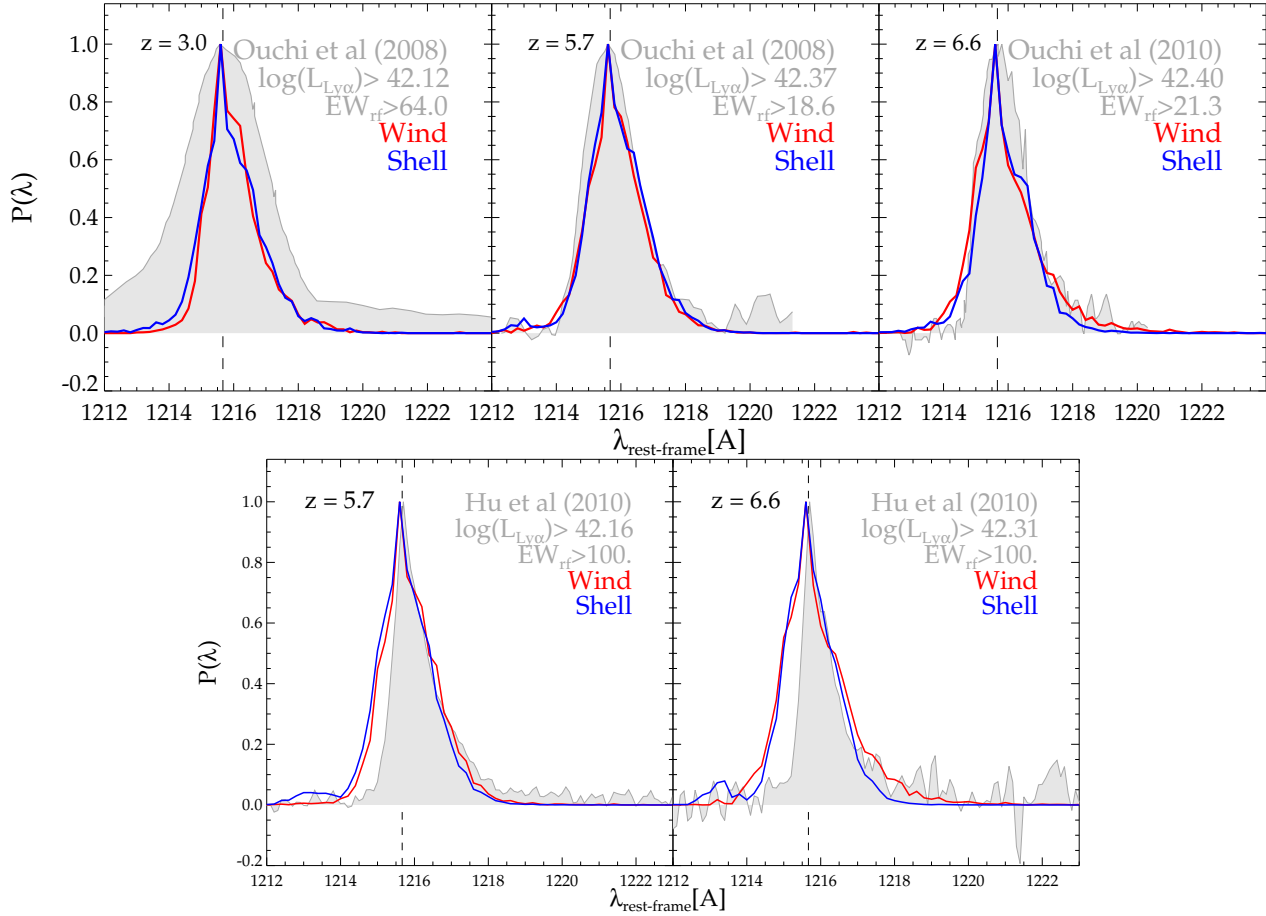


**Figure 13.** Composite Ly $\alpha$  line profiles of samples at different redshifts as indicated in each panel. The gray shaded regions show the Ly $\alpha$  line profiles from composite observational samples taken from Ouchi et al. (2008, 2010) and Hu et al. (2010) (as indicated in the legend of each box), whereas the solid curves show the model predictions using the Wind geometry (red) and the Shell geometry (blue). Galaxies in the models used to construct the composite spectra have been selected in the same way as the observed spectra, with the criteria shown in the legend of each box, where  $L_{Ly\alpha}$  is shown in units of  $[\text{erg s}^{-1} \text{ h}^{-2}]$  and the EW in  $\text{\AA}$ .

outflow geometries underpredict the fraction of Ly $\alpha$  emitters measured observationally. In particular, only at  $z > 5$  are the Wind and Shell geometries consistent with the fraction of Ly $\alpha$  emitters measured in the UV magnitude range  $-20.9 < M_{UV} - 5 \log(h) < -19.4$ .

Despite the differences, both outflow geometries predict an increase in the fraction of Ly $\alpha$  emitters with redshift, which is qualitatively consistent with the observations up to  $z \sim 6$ . At higher redshifts, the observational data of Schenker et al. (2011) and Pentericci et al. (2011) suggests a decline in the fraction of Ly $\alpha$  emitters at  $z \sim 7$ . They interpret this decline as the impact of the neutral IGM attenuating the Ly $\alpha$  luminosity from galaxies.

Our models, on the other hand, show a trend consistent to the observations in the magnitude range  $-19.4 < M_{UV} - 5 \log(h) < -17.9$ , except at the highest redshift,  $z = 7.3$  where both models increase their fraction of Ly $\alpha$  emitters instead of decreasing it, as observations do. However, it is worth noticing that in the UV magnitude range  $-20.9 < M_{UV} - 5 \log(h) < -19.4$  both outflow geometries predict a decline of the Ly $\alpha$  fraction similar to the one found observationally. Therefore, Fig. 12 shows that our model predictions imply that the decline in the Ly $\alpha$  fraction in LBG samples found at high redshifts is not conclusively driven by the presence of neutral HI in the IGM attenuating Ly $\alpha$  photons.

### 5.5 Observed Ly $\alpha$ line profiles

Observational measurements of individual and stacked line profiles of Ly $\alpha$  suggest the presence of outflows in galaxies (e.g. Shapley et al. 2003; Kashikawa et al. 2006; Dawson et al. 2007; Ouchi et al. 2008; Hu et al. 2010; Kornei et al. 2010; Ouchi et al. 2010; Steidel et al. 2010; Kulas et al. 2011). Ly $\alpha$  emitters can be characterised by studying the spectral features of the composite spectrum from a set of spectroscopic observations. The most prominent feature observed are asymmetric peaks, where the line is extended towards the red side. Other common spectral features are the appearance of a secondary peak and P-Cygni absorption features (see, e.g. Shapley et al. 2003).

In this section we compare our model predictions with the composite spectra of high redshift samples of Ly $\alpha$  emitters studied by Ouchi et al. (2008), Ouchi et al. (2010) and Hu et al. (2010). Based on the method used to construct composite spectra in the observational studies, we construct composite spectra in the model as follows. First, the Ly $\alpha$  profiles are normalised to their peak values. Then the spectrum is shifted so that the peaks coincide with the Ly $\alpha$  line centre,  $\lambda_{Ly\alpha} = 1216 \text{\AA}$ . Finally, the spectra are averaged at each wavelength bin.

The above method for constructing a composite spectrum has some important drawbacks. Since the redshift of Ly $\alpha$  emitters is

computed from the wavelength of the peak of the Ly $\alpha$  line, any offset of the peak due to radiative transfer effects is removed (see Fig. 1 and Fig. 2). On the other hand, the normalisation of the line profiles to the peak value can help enhance certain spectral features inherent to Ly $\alpha$  emitters by removing any dependence of the composite spectrum on Ly $\alpha$  luminosity. This also means that spectral features characteristic of a particular Ly $\alpha$  luminosity could be difficult to spot.

The top panels in Fig. 13 show a comparison between composite spectra at redshifts  $z = 3, 5.7$  and  $z = 6.6$  from Ouchi et al. (2008, 2010) with the predictions from both outflow geometries. Overall, both outflow geometries show very similar composite line profiles, regardless of redshift or limiting luminosity. A hint of a secondary peak redward of the line centre is weakly displayed for some configurations, but it is not strong enough to make a clear distinction between the line profiles predicted by both geometries.

The Ly $\alpha$  line in the composite spectrum estimated at  $z = 3.1$  by Ouchi et al. (2008) is broader than our model predictions. This could suggest that these galaxies have a larger column density or expansion velocity than our model predicts, as Fig. 2 also shows. At  $z = 5.7$  and  $z = 6.6$ , Fig. 13 shows remarkable agreement between the models and the observations by Ouchi et al. (2008) and Ouchi et al. (2010), respectively.

The situation is different when comparing with the composite spectra at  $z = 5.7$  and  $z = 6.6$  estimated by Hu et al. (2010). Their composite spectrum is constructed from samples of Ly $\alpha$  emitters of similar limiting Ly $\alpha$  luminosity but with  $EW_{\text{rf}} > 100\text{\AA}$ , significantly greater than the EW limit in the Ouchi et al. (2008) samples at  $z > 5$ , which have ( $EW_{\text{rf}} > 20\text{\AA}$ ).

In this case, the observational composite spectra are narrower than our model predictions. Moreover, the observed spectra appear to be more asymmetric than their counterparts in the Ouchi et al. (2008) and Ouchi et al. (2010) samples. The asymmetry of the Ly $\alpha$  line varies with the outflow expansion velocity, as discussed in Fig. 2.

It is interesting to notice that the composite spectra of Hu et al. (2010) show a sharp cut-off on their blue side, which is not well reproduced by our outflow geometries. This lack of photons in the blue side of the spectra could be interpreted as the impact of the IGM at these high redshifts removing the blue-side of the Ly $\alpha$  spectrum, as discussed by Dijkstra, Lidz & Wyithe (2007) and more recently by Laursen, Sommer-Larsen & Razoumov (2011). Since our outflow geometries do not show this feature, it seems likely to be caused by the presence of a neutral IGM. However, this does not explain the overall good agreement with the Ouchi et al. (2008) composite spectra at  $z = 5.7$  and the Ouchi et al. (2010) composite spectra at  $z = 6.6$ .

The predicted Ly $\alpha$  profiles shown in Fig. 13 show reasonable agreement with the data, thus supporting the idea that Ly $\alpha$  photons escape mainly through galactic outflows. It is worth reminding the reader that our outflow geometries are not tuned to reproduce the observed line shapes, and therefore these represent genuine predictions of the outflow geometries.

## 6 THE NATURE OF Ly $\alpha$ EMITTERS

After performing the detailed comparison between observational data and model predictions in the previous section, we conclude that our outflow geometries reproduce at some level the general features of the observations. We now turn to the question of what are the physical conditions that make a galaxy observable through

its Ly $\alpha$  emission. As previously shown in Fig. 12, only a fraction of UV-selected galaxies have detectable Ly $\alpha$  emission, implying that this selection targets galaxies with particular characteristics. To reveal the properties of Ly $\alpha$ -selected galaxies, we show in Fig. 14 a comparison between all galaxies and what we define here as a *typical* Ly $\alpha$  emitter, i.e. a galaxy with  $\log(L_{\text{Ly}\alpha}[\text{erg s}^{-1} \text{h}^{-2}]) \geq 41.5$  and  $EW_{\text{rf}} \geq 20\text{\AA}$ . This corresponds to a Ly $\alpha$  luminosity limit where Ly $\alpha$  emitters are abundant over the redshift range  $0.2 < z < 6.6$ , and the EW limit corresponds to a typical EW limit in observational samples. We use a top-hat filter centered on a rest-frame wavelength of  $\lambda = 1500\text{\AA}$  to ensure that the rest frame UV magnitude is the same for all redshifts.

The top row of Fig. 14 shows that, in general, both outflow geometries predict Ly $\alpha$  emitters at high redshift to have similar or somewhat lower metallicities than the bulk of the galaxy population at the same UV magnitude. At  $z = 0.2$ , however, the metallicity of Ly $\alpha$  emitters is larger than that of the overall galaxy population for a range of UV magnitudes.

The result that Ly $\alpha$  emitters have lower metallicities at higher redshifts than the overall galaxy population may not be surprising, since to first order we expect galaxies with low metallicities to have a low amount of dust and thus to be less attenuated in Ly $\alpha$  emission. However, according to Eq. (11), metallicity is not the only factor controlling the amount of dust, which is why our models predict that at some magnitudes, typical Ly $\alpha$  emitters can have the same (or even higher) metallicities than the bulk of the galaxy population.

Observational studies of the Ly $\alpha$  emitter population at  $z \sim 0.2$  have found that these galaxies have in general lower metallicities than the bulk of the galaxy population at the same stellar masses instead of UV magnitude (e.g. Finkelstein et al. 2011; Cowie, Barger & Hu 2010). At higher redshifts the same conclusion is drawn from the observational samples (see, e.g. Gawiser et al. 2006; Pentericci et al. 2007; Finkelstein et al. 2009). The metallicities our outflow geometries predict at different stellar masses cannot be directly compared with observational estimates, since these compute the stellar mass from SED fitting assuming a Salpeter or similar IMF. Our model, on the other hand, assumes a top-heavy IMF in starbursts, which are the dominant component of the Ly $\alpha$  emitter population in our model (see Fig. 6).

Historically, it was thought that metallicity was the main parameter driving the observability of the Ly $\alpha$  line, implying that Ly $\alpha$  emitters should be essentially metal-free galaxies (Meier & Terlevich 1981; Hartmann, Huchra & Geller 1984; Hartmann et al. 1988). Our model predictions, on the other hand, imply that the observability of the Ly $\alpha$  line depends on the interplay between more physical properties. Nevertheless, it is not the metallicity itself that determines the amount of dust that photons need to cross through when escaping. In our models, the dust optical depth depends both on the metallicity of the galaxies and on the hydrogen column density of the outflows, which is in turn a function of several properties, such as size, mass ejection rate, expansion velocity and cold gas content. Therefore, it is not surprising that Ly $\alpha$  emitters can be either metal-poor or metal-rich compared to the bulk of the galaxy population.

Fig. 14 also reveals that typical Ly $\alpha$  emitters in the Wind geometry have overall lower metallicities than their counterparts in the Shell geometry. This result is consistent with the higher sensitivity to dust in the Shell geometry compared with the Wind geometry, shown in Fig. 1. Due to the different response to dust of each model, it is natural that the predicted metallicities are correspondingly different.

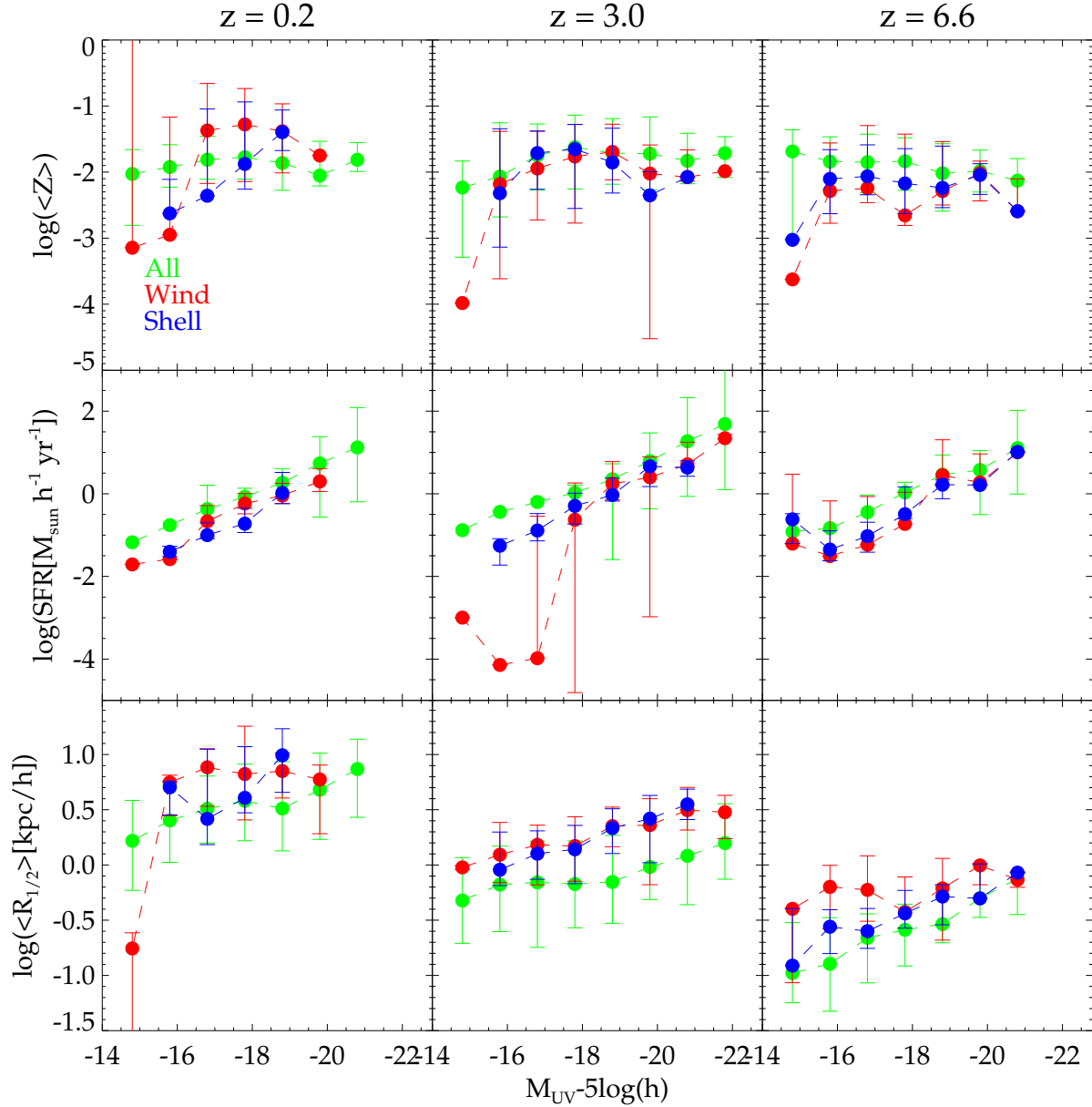


**Figure 14.** Galaxy properties as a function of extinguished  $UV$  magnitude for redshifts  $z = 0.2$  (left),  $z = 3.0$  (middle) and  $z = 6.6$  (right). Each row shows a different property. The top row shows the weighted metallicity of the cold gas, the middle row the instantaneous SFR, and the bottom row the half-mass radius. Green circles denote the median of the distribution including all galaxies per magnitude bin. Red and blue circles denote the median of the distribution of galaxies selected as *typical*  $Ly\alpha$  emitters (i.e. with  $\log(L_{Ly\alpha}[\text{erg s}^{-1} \text{ h}^{-2}]) \geq 41.5$  and  $EW \geq 20 \text{ \AA}$ ) in the Wind and Shell geometries, respectively. Error bars denote the 10-90 percentiles of the corresponding distribution.

Another clear difference between the overall galaxy population and  $Ly\alpha$  emitters is seen when looking at the instantaneous star formation rate at different  $UV$  magnitudes, shown in the middle panel of Fig. 14. Here it is clear that regardless of redshift or  $UV$  magnitude, both models predict that  $Ly\alpha$  emitters should have smaller SFRs than typical galaxies with the same  $UV$  magnitude.

The instantaneous SFR has an important impact on the escape of  $Ly\alpha$  photons in both models. In the Wind geometry, the mass ejection rate of the outflow depends directly on the SFR, as is clear from Eq. (13). The mass ejection rate is in turn directly proportional to the hydrogen column density of the outflows, according to Eq. (19), which in turn affects the path length of photons, the number of scatterings, and the amount of dust, as discussed previously.

Hence, a galaxy with a low SFR could have a high  $Ly\alpha$  escape fraction, making it observable. In the Shell geometry the SFR is also important, since it correlates with the cold gas mass, which in turn determines the hydrogen column density of the outflow.

Our outflow geometries are consistent with the observational evidence for  $Ly\alpha$  emitters having modest star formation rates (e.g. Gawiser et al. 2006; Gronwall et al. 2007; Guaita et al. 2010). However, it is worth remarking that our model predictions do not imply that  $Ly\alpha$  emitters have low SFRs, but instead have lower SFRs than the bulk of the galaxy population at the same  $UV$  magnitude. As shown in the previous section,  $Ly\alpha$  emitters at high redshifts are predicted to be mainly starbursts.

Finally, we also study the difference in the size of galaxies,

since our outflow geometries depend strongly on the galaxy half-mass radius. In the Wind geometry, the hydrogen column density scales as  $\sim \langle R_{1/2} \rangle^{-1}$ , and in the Shell geometry the hydrogen column density scales as  $\sim \langle R_{1/2} \rangle^{-2}$ . In order to obtain a high Ly $\alpha$  escape fraction,  $N_H$  has to be low in general, and this could be attained by having a large  $\langle R_{1/2} \rangle$ . Hence, not surprisingly, our outflow geometries predict that Ly $\alpha$  emitters typically have larger sizes than the bulk of the galaxy population. This result is independent of redshift and UV magnitude, although in detail the difference in sizes may vary with these quantities. A similar result is reported by Bond et al. (2009) at  $z = 3$ . They find the sizes of Ly $\alpha$  emitters (in Ly $\alpha$  emission) to be always smaller than  $\sim 3\text{ kpc/h}$ , consistent with the half-mass radius of our typical Ly $\alpha$  emitters at this redshift.

## 7 SUMMARY AND CONCLUSIONS

In this paper we couple the galaxy properties predicted by the Baugh et al. (2005) version of the semianalytical model GALFORM with a Monte Carlo radiative transfer model of the escape of Ly $\alpha$  photons to study the properties of Ly $\alpha$  emitters in a cosmological context.

Motivated by observational evidence that galactic outflows shape the asymmetric profiles of the Ly $\alpha$  line, we developed two different outflow geometries, each defined using the predicted properties of galaxies in GALFORM in a slightly different way. Our Shell geometry, which consists of an expanding thin spherical shell, has a column density  $N_H$  proportional to the cold gas mass in the ISM of galaxies. Our Wind geometry, on the other hand, consists of a spherical expanding wind with number density that decreases with increasing radius. The column density in the Wind geometry is related to the mass ejection rate from supernovae, which is computed by GALFORM.

We study in detail the Ly $\alpha$  line profiles and characterise them in terms of their width, asymmetry and offset with respect to the line centre, as a function of the outflow column density, expansion velocity and metallicity. The Ly $\alpha$  properties of the outflow geometries we study are found to be sensitive to the column density, expansion velocity and the geometry of the outflows, as shown in Fig. 2. Metallicity is found to have a smaller impact on the line profiles, although it has a great impact on the Ly $\alpha$  escape fraction, as shown in Fig. 3.

Both the width and offset from the line centre are found to increase for outflows with increasing column densities and expansion velocities. In both cases, the Ly $\alpha$  line profiles in the Shell geometry are more affected by changes of these properties than the Wind geometry.

The Ly $\alpha$  escape fraction is found to decrease with metallicity and column density, since those two properties are directly proportional to the optical depth of absorption. Also, higher values of the expansion velocity tend to increase the escape fraction. This rather complicated interplay between the column density, expansion velocity, metallicity and geometry justifies our choice for computing the Ly $\alpha$  escape fraction from a fully-fledged Ly $\alpha$  radiative transfer model instead of imposing a phenomenological model.

The drawback is, of course, the difficulty in coupling both models in order to obtain a Ly $\alpha$   $f_{\text{esc}}$  for each galaxy predicted by GALFORM. One critical step is to choose the free parameters in our models. In order to set these for each model, we attempt to fit the observed cumulative luminosity function of Ly $\alpha$  emitters over the redshift range  $0 < z < 7$ . We find that a single

choice of parameters applied at all redshifts cannot reproduce the observed CLFs. Motivated by the observed difference in sizes between the star forming regions in local and high redshift starbursts (e.g. Rujopakarn et al. 2011), we allow the outflow radii in our models to evolve with redshift when the galaxies are starbursts. By doing this we can find a suitable combination of parameters to match the measured Ly $\alpha$  CLF.

It is worth pointing out that the need to invoke a redshift dependence in the outflow sizes in starbursts could suggest that other important physical processes which determine the escape of Ly $\alpha$  photons may not be included in this work. Although outflows have been proposed in the past as a mechanism to boost the otherwise very low escape fraction of Ly $\alpha$  photons, other scenarios have been proposed. A clumpy ISM could boost the escape of Ly $\alpha$  photons with respect to that of Lyman continuum photons, since the former have a probability of bouncing off a dust cloud, and therefore have more chances to escape, whereas in the latter case photons travel through dust clouds, and hence have more chances of being absorbed (Neufeld 1991; Hansen & Oh 2006).

Another physical effect not included in our modelling is the attenuation of Ly $\alpha$  radiation due to the scattering of Ly $\alpha$  photons when crossing regions of neutral hydrogen in the IGM. This effect has been shown to be important at  $z \gtrsim 6$  when the fraction of neutral hydrogen in the IGM is thought to have been significant (see, e.g. Dijkstra, Lidz & Wyithe 2007; Dayal, Ferrara & Saro 2010; Dijkstra, Mesinger & Wyithe 2011; Laursen, Sommer-Larsen & Razoumov 2011). Hence, we do not expect this to significantly change our model predictions at low redshifts.

A more fundamental uncertainty lies in the calculation of the *intrinsic* Ly $\alpha$  luminosity of galaxies, which does not depend upon the radiative transfer modelling. We can assess whether GALFORM computes the correct intrinsic Ly $\alpha$  luminosity by studying the intrinsic (unattenuated) H $\alpha$  luminosity function, since both emission-line luminosities are directly related to the production rate of Lyman continuum photons (see Orsi et al. 2010), and differ only by their case B recombination emission coefficient (Osterbrock 1989). Moreover, the H $\alpha$  emission from galaxies is less sensitive to dust than Ly $\alpha$  since these photons do not undergo multiple scatterings in the ISM, making their path lengths shorter than the typical path lengths Ly $\alpha$  photons experience, and thus making it easier to estimate their attenuation by dust.

The attenuation by dust can be estimated by computing the ratio of the intensity of two or more emission lines and comparing with the expectation for case B recombination (see, for example, Kennicutt 1983, 1998). By comparing observed dust-attenuated H $\alpha$  LFs with GALFORM predictions (Orsi et al. 2010) we have found that, at  $z \sim 0.2$ , GALFORM roughly overestimates the intrinsic H $\alpha$  luminosities by a factor  $\sim 3$ . The scatter in the observed H $\alpha$  luminosity functions is large, making it difficult to estimate this accurately. Nevertheless, the intrinsic Ly $\alpha$  luminosities predicted at  $z = 0.2$  are a factor  $\sim 10$  or more brighter than what is needed to reproduce the observational results, if we fix the free parameters of the outflow geometries, meaning that the uncertainty in the intrinsic Ly $\alpha$  luminosity is not solely responsible for the discrepancy between the observed and predicted LFs.

Despite this, our simple outflow geometries are found to be in agreement with a set of different observations, implying that our modelling does reproduce the basic physical conditions determining the escape of Ly $\alpha$  photons from galaxies.

A direct prediction of our outflow geometries is the distribution of hydrogen column densities of Ly $\alpha$  emitters. We find that



both models feature column densities with values ranging from  $N_H \sim 10^{19} - 10^{23} [\text{cm}^{-2}]$ , which is consistent with observational estimates shown in Verhamme et al. (2008). The column density distribution is closely related to the predicted Ly $\alpha$  escape fractions. We find that bright Ly $\alpha$  emitters generally have high escape fractions, and faint Ly $\alpha$  emitters have low escape fractions. An important consequence of this is that certain galaxy properties which correlate with the intrinsic Ly $\alpha$  luminosity (such as the instantaneous SFR) do not correlate in a simple way with the observed Ly $\alpha$  luminosity. In other words, galaxies with the same intrinsic Ly $\alpha$  luminosity (or, say, the same SFR) could be observed with different Ly $\alpha$  luminosities, making the interpretation of the properties of Ly $\alpha$  emitters complicated.

The predicted escape fractions in the models are remarkably consistent with observational measurements (Fig. 9), giving further support to the scenario of Ly $\alpha$  photons escaping through galactic outflows. Although the Wind geometry is only partially consistent with the observed escape fractions, it is worth pointing out that the observational data used to make the comparison in Fig. 9 does not constitute a representative sample of the galaxy population at this redshift.

Since our Monte Carlo radiative transfer model records the frequency with which photons escape from an outflow, we make use of this information to study the predicted Ly $\alpha$  line profiles from our outflow geometries and compare them with observational measurements. In some cases the agreement is remarkably good, but in others we find significant differences (see Fig. 13). A detailed study of the line profiles could reveal important information about the galaxy properties. We plan to undertake such a study of Ly $\alpha$  line profiles in the context of a galaxy formation model in a future paper.

Finally, our models predict that only a small fraction of galaxies should be selected as Ly $\alpha$  emitters. We illustrate in Fig. 14 that Ly $\alpha$  emitters are found in general to have low metallicities (except at  $z = 0.2$ ), low instantaneous SFR and large sizes, compared to the overall galaxy population. These constraints arise naturally as a consequence of the radiative transfer modelling incorporated in GALFORM in this paper. Galaxies need to have low star formation rates and large sizes in order to display an outflow with a small column density. Since the dust content depends on the optical depth of dust and not the metallicity alone, Ly $\alpha$  emitters are not necessarily low-metallicity galaxies in our models.

The models presented here for the emission of Ly $\alpha$  represent an important step towards a detailed understanding of the physical properties of these galaxies. With the advent of large observational campaigns in the forthcoming years focusing on detecting Ly $\alpha$  emitters at high redshifts, new data will help us refine and improve our physical understanding of these galaxies, and thus, enable us to improve our knowledge of galaxy formation and evolution, particularly in the high redshift Universe.

## ACKNOWLEDGEMENTS

AO acknowledges a STFC-Gemini scholarship. This work was supported in part by Proyecto Gemini 320900212 and an STFC rolling grant. We thank Peter Laursen for making data from the MoCaLaTA radiative transfer code available for us to test our code, and Nelson Padilla for useful comments and discussions. Part of the calculations for this work were performed using the Geryon supercomputer at AIUC.

## REFERENCES

- Ahn S., 2003, *Journal of Korean Astronomical Society*, 36, 145  
—, 2004, *ApJ*, 601, L25  
Ahn S.-H., Lee H.-W., Lee H. M., 2000, *Journal of Korean Astronomical Society*, 33, 29  
Atek H., Kunth D., Hayes M., Östlin G., Mas-Hesse J. M., 2008, *A&A*, 488, 491  
Atek H., Kunth D., Schaerer D., Hayes M., Deharveng J. M., Östlin G., Mas-Hesse J. M., 2009, *A&A*, 506, L1  
Barnes L. A., Haehnelt M. G., 2010, *MNRAS*, 403, 870  
Baugh C. M., 2006, *Reports on Progress in Physics*, 69, 3101  
Baugh C. M., Lacey C. G., Frenk C. S., Granato G. L., Silva L., Bressan A., Benson A. J., Cole S., 2005, *MNRAS*, 356, 1191  
Benson A. J., Bower R. G., Frenk C. S., Lacey C. G., Baugh C. M., Cole S., 2003, *ApJ*, 599, 38  
Benson A. J., Lacey C. G., Baugh C. M., Cole S., Frenk C. S., 2002, *MNRAS*, 333, 156  
Blanc G. A. et al., 2011, *ApJ*, 736, 31  
Bolton J. S., Haehnelt M. G., 2007, *MNRAS*, 382, 325  
Bond N. A., Gawiser E., Gronwall C., Ciardullo R., Altmann M., Schawinski K., 2009, *ApJ*, 705, 639  
Bower R. G., Benson A. J., Malbon R., Helly J. C., Frenk C. S., Baugh C. M., Cole S., Lacey C. G., 2006, *MNRAS*, 370, 645  
Cardelli J. A., Clayton G. C., Mathis J. S., 1989, *ApJ*, 345, 245  
Cen R., 1992, *ApJS*, 78, 341  
Charlot S., Fall S. M., 1993, *ApJ*, 415, 580  
Cole S., Lacey C. G., Baugh C. M., Frenk C. S., 2000, *MNRAS*, 319, 168  
Cowie L. L., Barger A. J., Hu E. M., 2010, *ApJ*, 711, 928  
Cowie L. L., Hu E. M., 1998, *AJ*, 115, 1319  
Cowie L. L., Hu E. M., Songaila A., 2011, *ApJ*, 735, L38+  
Dawson S., Rhoads J. E., Malhotra S., Stern D., Wang J., Dey A., Spinrad H., Jannuzi B. T., 2007, *ApJ*, 671, 1227  
Dayal P., Ferrara A., Gallerani S., 2008, *MNRAS*, 389, 1683  
Dayal P., Ferrara A., Saro A., 2010, *MNRAS*, 402, 1449  
Dayal P., Maselli A., Ferrara A., 2011, *MNRAS*, 410, 830  
Deharveng J. et al., 2008, *ApJ*, 680, 1072  
Dijkstra M., Haiman Z., Spaans M., 2006, *ApJ*, 649, 14  
Dijkstra M., Lidz A., Wyithe J. S. B., 2007, *MNRAS*, 377, 1175  
Dijkstra M., Mesinger A., Wyithe J. S. B., 2011, *MNRAS*, 414, 2139  
Finkelstein S. L., Cohen S. H., Moustakas J., Malhotra S., Rhoads J. E., Papovich C., 2011, *ApJ*, 733, 117  
Finkelstein S. L., Rhoads J. E., Malhotra S., Grogin N., 2009, *ApJ*, 691, 465  
Forero-Romero J. E., Yepes G., Gottlöber S., Knollmann S. R., Cuesta A. J., Prada F., 2011, *MNRAS*, 415, 3666  
Franke H., 2009, *New Astronomical Reviews*, 53, 47  
Frank A., 1999, *New Astronomical Reviews*, 43, 31  
Gawiser E. et al., 2007, *ApJ*, 671, 278  
—, 2006, *ApJS*, 162, 1  
Giavalisco M., Koratkar A., Calzetti D., 1996, *ApJ*, 466, 831  
Gonzalez J. E., Lacey C. G., Baugh C. M., Frenk C. S., Benson A. J., 2011, *ArXiv e-prints*, 11053731  
Granato G. L., Lacey C. G., Silva L., Bressan A., Baugh C. M., Cole S., Frenk C. S., 2000, *ApJ*, 542, 710  
Gronwall C. et al., 2007, *ApJ*, 667, 79  
Guaita L. et al., 2011, *ApJ*, 733, 114  
—, 2010, *ApJ*, 714, 255  
Haardt F., Madau P., 1996, *ApJ*, 461, 20  
—, 2001, in *Clusters of Galaxies and the High Redshift Universe*



- Observed in X-rays, D. M. Neumann & J. T. V. Tran, ed.  
Hansen M., Oh S. P., 2006, MNRAS, 367, 979  
Harrington J. P., 1973, MNRAS, 162, 43  
Hartmann L. W., Huchra J. P., Geller M. J., 1984, ApJ, 287, 487  
Hartmann L. W., Huchra J. P., Geller M. J., O'Brien P., Wilson R., 1988, ApJ, 326, 101  
Hayes M. et al., 2010, Nature, 464, 562  
Hayes M., Schaerer D., Östlin G., Mas-Hesse J. M., Atek H., Kunth D., 2011, ApJ, 730, 8  
Heney L. G., Greenstein J. L., 1941, ApJ, 93, 70  
Hjerting F., 1938, ApJ, 88, 508  
Hu E. M., Cowie L. L., Barger A. J., Capak P., Kakazu Y., Trouille L., 2010, ApJ, 725, 394  
Hu E. M., Cowie L. L., McMahon R. G., Capak P., Iwamuro F., Kneib J., Maihara T., Motohara K., 2002, ApJ, 568, L75  
Hummer D. G., 1962, MNRAS, 125, 21  
Iono D. et al., 2009, ApJ, 695, 1537  
Kashikawa N. et al., 2006, ApJ, 648, 7  
Kennicutt, Jr. R. C., 1983, ApJ, 272, 54  
—, 1998, ARA&A, 36, 189  
Kobayashi M. A. R., Totani T., Nagashima M., 2007, ApJ, 670, 919  
—, 2010, ApJ, 708, 1119  
Kornei K. A., Shapley A. E., Erb D. K., Steidel C. C., Reddy N. A., Pettini M., Bogosavljević M., 2010, ApJ, 711, 693  
Kovač K., Somerville R. S., Rhoads J. E., Malhotra S., Wang J., 2007, ApJ, 668, 15  
Kudritzki R. et al., 2000, ApJ, 536, 19  
Kulas K. R., Shapley A. E., Kollmeier J. A., Zheng Z., Steidel C. C., Hainline K. N., 2011, ArXiv e-prints, 11074367  
Kunth D., Mas-Hesse J. M., Terlevich E., Lequeux J., Fall S. M., 1998, A&A, 334, 11  
Lacey C. G., Baugh C. M., Frenk C. S., Benson A. J., 2011, MNRAS, 45  
Lacey C. G., Baugh C. M., Frenk C. S., Silva L., Granato G. L., Bressan A., 2008, MNRAS, 385, 1155  
Lagos C. D. P., Lacey C. G., Baugh C. M., Bower R. G., Benson A. J., 2011, MNRAS, 416, 1566  
Laursen P., Razoumov A. O., Sommer-Larsen J., 2009, ApJ, 696, 853  
Laursen P., Sommer-Larsen J., 2007, ApJ, 657, L69  
Laursen P., Sommer-Larsen J., Razoumov A. O., 2011, ApJ, 728, 52  
Le Delliou M., Lacey C., Baugh C. M., Guiderdoni B., Bacon R., Courtois H., Sousbie T., Morris S. L., 2005, MNRAS, 357, L11  
Le Delliou M., Lacey C. G., Baugh C. M., Morris S. L., 2006, MNRAS, 365, 712  
Loeb A., Rybicki G. B., 1999, ApJ, 524, 527  
Mas-Hesse J. M., Kunth D., Atek H., Östlin G., Leitherer C., Petrosian A., Schaerer D., 2009, Ap&SS, 320, 35  
Mas-Hesse J. M., Kunth D., Tenorio-Tagle G., Leitherer C., Terlevich R. J., Terlevich E., 2003, ApJ, 598, 858  
Meier D. L., Terlevich R., 1981, ApJ, 246, L109  
Meiksin A. A., 2009, Reviews of Modern Physics, 81, 1405  
Nagamine K., Cen R., Furlanetto S. R., Hernquist L., Night C., Ostriker J. P., Ouchi M., 2006, New Astronomy Review, 50, 29  
Nagamine K., Ouchi M., Springel V., Hernquist L., 2010, PASJ, 62, 1455  
Neufeld D. A., 1990, ApJ, 350, 216  
—, 1991, ApJ, 370, L85  
Nilsson K. K., Möller-Nilsson O., Möller P., Fynbo J. P. U., Shapley A. E., 2009, MNRAS, 400, 232  
Orsi A., Baugh C. M., Lacey C. G., Cimatti A., Wang Y., Zamorani G., 2010, MNRAS, 405, 1006  
Orsi A., Lacey C. G., Baugh C. M., Infante L., 2008, MNRAS, 391, 1589  
Osterbrock D. E., 1989, Astrophysics of gaseous nebulae and active galactic nuclei, Osterbrock, D. E., ed.  
Östlin G., Hayes M., Kunth D., Mas-Hesse J. M., Leitherer C., Petrosian A., Atek H., 2009, AJ, 138, 923  
Ouchi M. et al., 2008, ApJS, 176, 301  
—, 2010, ApJ, 723, 869  
Peebles P. J. E., 1993, Principles of physical cosmology, Peebles, P. J. E., ed.  
Pentericci L. et al., 2011, ArXiv e-prints, 11071376  
Pentericci L., Grazian A., Fontana A., Salimbeni S., Santini P., de Santis C., Gallozzi S., Giallongo E., 2007, A&A, 471, 433  
Rauch M. et al., 2008, ApJ, 681, 856  
Rhoads J. E., Malhotra S., Dey A., Stern D., Spinrad H., Jannuzi B. T., 2000, ApJ, 545, L85  
Rujopakarn W., Rieke G. H., Eisenstein D. J., Juneau S., 2011, ApJ, 726, 93  
Schaerer D., 2007, ArXiv e-prints, 07060139  
Schenker M. A., Stark D. P., Ellis R. S., Robertson B. E., Dunlop J. S., McLure R. J., Kneib J., Richard J., 2011, ArXiv e-prints, 11071261  
Shapley A. E., Steidel C. C., Pettini M., Adelberger K. L., 2003, ApJ, 588, 65  
Shimasaku K. et al., 2006, PASJ, 58, 313  
Silva L., Granato G. L., Bressan A., Danese L., 1998, ApJ, 509, 103  
Stark D. P., Ellis R. S., Chiu K., Ouchi M., Bunker A., 2010, MNRAS, 408, 1628  
Steidel C. C., Bogosavljević M., Shapley A. E., Kollmeier J. A., Reddy N. A., Erb D. K., Pettini M., 2011, ApJ, 736, 160  
Steidel C. C., Erb D. K., Shapley A. E., Pettini M., Reddy N., Bogosavljević M., Rudie G. C., Rakic O., 2010, ApJ, 717, 289  
Strickland D., 2002, in Astronomical Society of the Pacific Conference Series, Vol. 253, Chemical Enrichment of Intracluster and Intergalactic Medium, R. Fusco-Femiano & F. Matteucci, ed., pp. 387–+  
Thuan T. X., Izotov Y. I., 1997, ApJ, 489, 623  
Tilvi V., Malhotra S., Rhoads J. E., Scannapieco E., Thacker R. J., Iliev I. T., Mellema G., 2009, ApJ, 704, 724  
Tilvi V. et al., 2010, ApJ, 721, 1853  
Verhamme A., Schaerer D., Atek H., Tapken C., 2008, A&A, 491, 89  
Verhamme A., Schaerer D., Maselli A., 2006, A&A, 460, 397  
Zheng Z., Cen R., Trac H., Miralda-Escudé J., 2010, ApJ, 716, 574  
—, 2011, ApJ, 726, 38  
Zheng Z., Miralda-Escudé J., 2002, ApJ, 578, 33

## APPENDIX A: DESCRIPTION OF THE MONTE CARLO RADIATIVE TRANSFER CODE

In the context of Ly $\alpha$  radiative transfer, photon frequencies,  $\nu$ , are usually expressed in terms of Doppler units  $x$ , given by Eq. (20). The thermal velocity dispersion of the gas,  $v_{\text{th}}$ , is given by

$$v_{\text{th}} = \left( \frac{2k_B T}{m_p} \right)^{1/2}, \quad (\text{A1})$$

where  $k_B$  is the Boltzmann constant,  $T$  is the gas temperature,  $m_p$  is the proton mass and  $\nu_0$  is the central frequency of the Ly $\alpha$  line,  $\nu_0 = 2.47 \times 10^{15}$  Hz.

When a Ly $\alpha$  photon interacts with a hydrogen atom, the scattering cross section in the rest frame of the atom is given by

$$\sigma_\nu = f_{12} \frac{\pi e^2}{m_e c} \frac{\Gamma/4\pi^2}{(\nu - \nu_0)^2 + (\Gamma/4\pi)^2}, \quad (\text{A2})$$

where  $f_{12} = 0.4162$  is the Ly $\alpha$  oscillator frequency, and  $\Gamma = A_{12} = 6.25 \times 10^8 \text{ s}^{-1}$  is the Einstein coefficient for the Ly $\alpha$  transition ( $n = 2$  to  $n = 1$ ).

The optical depth of a Ly $\alpha$  photon with frequency  $\nu$  is determined by convolving this cross section with the velocity distribution of the gas,

$$\tau_\nu(s) = \int_0^s \int_{-\infty}^{+\infty} n(V_z) \sigma(\nu, V_z) dV_z dl, \quad (\text{A3})$$

where  $V_z$  denotes the velocity component along the photon's direction. Atoms are assumed to have a Maxwell-Boltzmann velocity distribution in the rest frame of the gas. In Doppler units, the optical depth can be written as

$$\tau_x(s) = \sigma_H(x) n_H s = 5.868 \times 10^{-14} T_4^{-1/2} N_H \frac{H(x, a)}{\sqrt{\pi}}, \quad (\text{A4})$$

where  $n_H$  is the hydrogen density,  $N_H$  the corresponding hydrogen column density,  $T_4$  the temperature in units of  $10^4 \text{ K}$  and  $a$  is the Voigt parameter, defined as

$$a = \frac{\Gamma/4\pi}{\Delta\nu_D} = 4.7 \times 10^{-4} T_4^{-1/2} \quad (\text{A5})$$

The Hjerting function  $H(x, a)$  (Hjerting 1938) describes the Voigt scattering profile,

$$H(x, a) = \frac{a}{\pi} \int_{-\infty}^{+\infty} \frac{e^{-y^2} dy}{(y - x)^2 + a^2}, \quad (\text{A6})$$

which is often approximated by a central resonant core and power-law “damping wings” for frequencies  $|x|$  below/above a certain boundary frequency  $x_c$ , which typically ranges between  $2.5 < x_c < 4$ . As a consequence, photons with frequencies close to the line centre have a large scattering cross section compared to those with frequencies in the wings of the profile. Hence, photons will be more likely to escape a medium when they have a frequency away from the line centre.

Scattering events are considered to be *coherent* (the frequency of the photon is the same before and after the scattering event) only in the rest frame of the atom, but not in the observer's frame. Thus, the thermal motion of the atom, plus any additional bulk motion of the gas, will potentially Doppler shift the frequency of the photons, giving them the chance to escape from the resonant core.

In the following,  $\xi_1, \xi_2, \xi_3, \dots$  are different random numbers in the range  $[0, 1]$ .

The location of the interaction (with either a dust grain or a hydrogen atom) is calculated as follows. The optical depth  $\tau_{\text{int}}$  the photon will travel is determined by sampling the probability distribution

$$P(\tau) = 1 - e^{-\tau}, \quad (\text{A7})$$

and so

$$\tau_{\text{int}} = -\ln(1 - \xi_1). \quad (\text{A8})$$

This optical depth corresponds to a distance travelled  $s$  given by

$$\tau(s) = \tau_x(s) + \tau_d(s), \quad (\text{A9})$$

where  $\tau_x(s)$  and  $\tau_d(s)$  are the optical depths due to hydrogen atoms and dust grains respectively. The length of the path travelled is determined by finding the distance  $s$  where  $\tau(s) = \tau_{\text{int}}$  by setting

$$s = \frac{\tau_{\text{int}}}{n_H \sigma_x + n_d \sigma_d}, \quad (\text{A10})$$

where  $n_d$  and  $\sigma_d$ , the number density of dust grains and cross-section for interaction with dust, are described below.

The new location of the photon corresponds to the point where it interacts with either a hydrogen atom or a dust grain. To find out which type of interaction the photon experiences, we compute the probability  $P_H(x)$  of being scattered by a hydrogen atom, given by

$$P_H(x) = \frac{n_H \sigma_H(x)}{n_H \sigma_H(x) + n_d \sigma_d}. \quad (\text{A11})$$

We generate a random number  $\xi_2$  and compare it to  $P_H$ . If  $\xi_2 < P_H$ , then the photon interacts with the hydrogen atom, otherwise, it interacts with dust.

When interacting with a dust grain, a Ly $\alpha$  photon can be either absorbed or scattered. This depends on the albedo of dust particles. At the wavelength of Ly $\alpha$ , the albedo is  $A \sim 0.4$ , depending on the extinction curve used. If the Ly $\alpha$  photon is absorbed, then it is lost forever. If not, then it will be scattered. The new direction will depend on a probability distribution for the elevation angle  $\theta$ , whereas for the azimuthal angle  $\phi$  the scattering will be uniformly distributed. The scattering angle  $\theta$  can be obtained from the Henyey & Greenstein (1941) phase function

$$P_{HG}(\mu) = \frac{1}{2} \frac{1 - g^2}{(1 + g^2 - 2g\mu)^{3/2}}, \quad (\text{A12})$$

where  $\mu = \cos \theta$  and  $g = \langle \mu \rangle$  is the asymmetry parameter. If  $g = 0$ , Eq.(A12) reduces to isotropic scattering.  $g = 1(-1)$  implies complete forward (backward) scattering. In general  $g$  depends on the wavelength. For Ly $\alpha$  photons,  $g = 0.73$ .

If the photon is interacting with dust, then we generate a random number  $\xi_3$  to determine whether it is going to be absorbed or scattered, comparing this number to  $A$ . If the photon is absorbed, then it is lost. If it is scattered, then a new direction must be drawn.

The interaction of photons with hydrogen atoms is more complicated. Inside an HI region, atoms move in random directions with velocities given by the Maxwell-Boltzmann distribution. Each of these atoms will *see* the same photon moving with a different frequency, due to the Doppler shift caused by their velocities. Since the cross section for scattering depends on the frequency of the photon, the probability for an atom to interact with a photon will depend on a combination of the frequency of the photon and the velocity of the atom.

To compute the direction of the photon after the scattering event, a Lorentz transformation to the frame of the atom must be made. The direction of the photon in this frame,  $\mathbf{n}'_o$ , is given by a dipole distribution, with the symmetry axis defined by the incident direction  $\mathbf{n}'_i$

$$P(\theta) = \frac{3}{8} (1 + \cos^2 \theta), \quad (\text{A13})$$

where  $\theta$  is the polar angle to the direction  $\mathbf{n}'_i$ . The azimuthal angle of the outgoing photon is uniformly distributed in the range  $0 \leq \phi < 2\pi$ . With a Lorentz transformation back to the frame of the medium we obtain  $\mathbf{n}_o$ , the new direction of the photon. Finally, the

new frequency of the photon is given by

$$x_f = x - \mathbf{n}_i \cdot \mathbf{u} + \mathbf{n}_o \cdot \mathbf{u}, \quad (\text{A14})$$

$$= x - u_{\parallel} + \mathbf{n}_o \cdot \mathbf{u}, \quad (\text{A15})$$

where  $\mathbf{u} = \mathbf{v}/v_{\text{th}}$  is the velocity of the hydrogen atom in units of the thermal velocity, and  $u_{\parallel}$  is the atom's velocity component along the photon's direction prior to the scattering event.

The algorithm described above will follow the scattering of a photon until it escapes (or is absorbed), and then the process starts again with a new photon traveling on a different path, and so on until we are satisfied with the number of photons generated. In practice, for the runs shown in this paper the number of photons generated varies between a few thousand up to several hundred thousand, depending on the accuracy of the result we wish to achieve.

For the typical HI regions studied here, the number of scatterings that photons undergo before escaping could be as high as several tens or hundreds of millions. If we want to model several thousand photons, then the total number of calculations grows enormously and the task becomes computationally infeasible. However, most of the scattering events will occur when the photon is at the line centre, or very close to it, where the cross section for scattering peaks. Whenever the photon falls near the centre it will experience so many scatterings that the actual distance travelled between each scattering event will be negligible, since in this case it will most likely be scattered by an atom with a velocity close to zero. Hence, the frequency after such scattering will remain in the resonant core. This motivates the possibility of accelerating the code performance by skipping such *inconsequential* scattering events.

Following Dijkstra, Haiman & Spaans (2006), a critical frequency,  $x_{\text{crit}}$ , defines a transition from the resonant core to the wing. Whenever a photon is in the core (with  $|x| < x_{\text{crit}}$ ) we can push it to the wings by allowing the photon to be scattered only by a rapidly moving atom. We do this by modifying the distribution of perpendicular velocities by a *truncated* Gaussian, i.e. a distribution which is a Gaussian for  $|u| > x_{\text{crit}}$  but zero otherwise. The modified perpendicular velocities are then drawn from

$$u_{\perp 1} = \sqrt{x_{\text{crit}}^2 - \ln(\xi_4)} \cos(2\pi\xi_2) \quad (\text{A16})$$

$$u_{\perp 2} = \sqrt{x_{\text{crit}}^2 - \ln(\xi_4)} \sin(2\pi\xi_2). \quad (\text{A17})$$

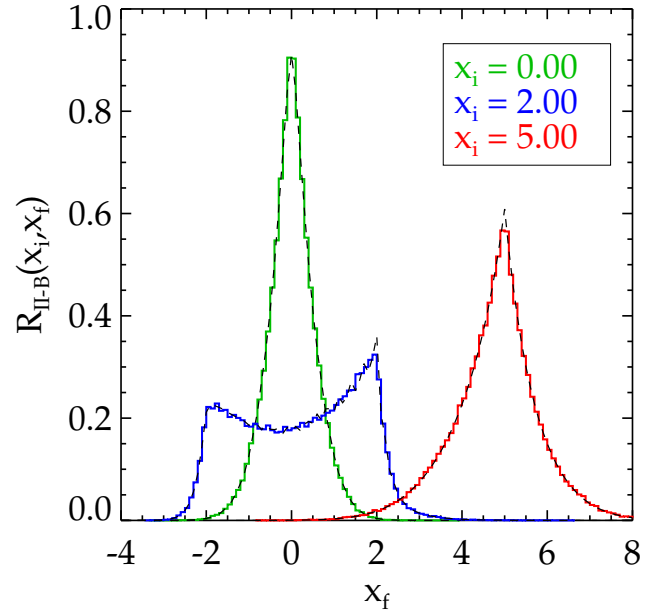
When doing this, we allow the photon to redshift or blueshift away from the line centre, thus reducing the cross section for scattering and increasing the path length. For the configurations studied here, we found that a value of  $x_{\text{crit}} = 3$  provides a good balance between accuracy and efficiency of the code, reducing the execution time by a factor 100 or more with respect to the non-accelerated case.

### A1 Validation of the radiative transfer code

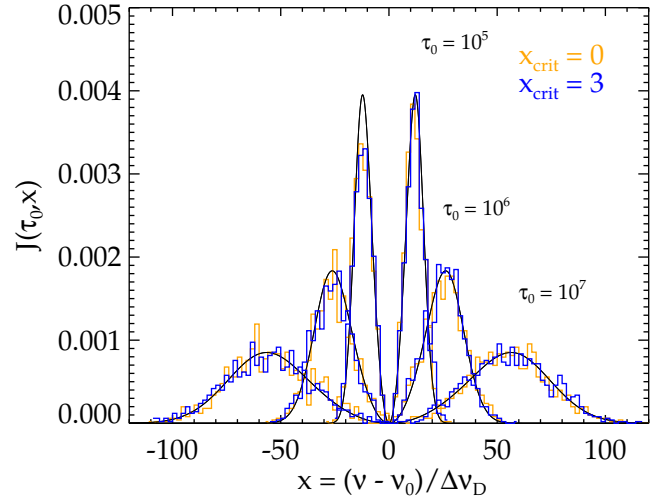
The flexibility of our Monte Carlo radiative transfer code allows us to reproduce configurations for which analytical solutions are available. Hence, these are ideal to test the performance and accuracy of the code. In the following we describe the tests we have performed on our code, where each comparison with an analytical solution tests a different aspect of the code.

Fig. A1 shows the resulting redistribution function for 3 different initial frequencies using  $\sim 10^5$  photons. There is a remarkably good agreement between the Monte Carlo code and the analytical expression of Hummer (1962) for coherent scattering with a dipolar angular distribution, including radiation damping.

The emergent spectrum from an optically thick, homogeneous



**Figure A1.** The redistribution function of Ly $\alpha$  photons scattered by hydrogen atoms for different initial frequencies. The histograms show the resulting frequency distribution from the Monte Carlo code, whereas the dashed lines show a numerical integration of the analytical solution of Hummer (1962).



**Figure A2.** Ly $\alpha$  spectrum emerging from a homogeneous static slab at  $T = 10\text{K}$ , for optical depths at the line centre of  $\tau_0 = 10^5, 10^6$  and  $10^7$ , as shown in the plot. The profiles are symmetric around  $x = 0$ . The more optically thick the medium, the farther from the line centre the resulting peaks of each profile are found. The solid lines show the analytical solution by Harrington (1973), and the orange and blue histograms show the results from the Monte Carlo code for a choice of  $x_{\text{crit}} = 0$  and 3, respectively.

static slab with photons generated at the line centre was first calculated by Harrington (1973), and the result was generalised by Neufeld (1990), allowing the generated photons to have any frequency.

Fig. A2 shows the emergent spectrum from a simulated homogeneous slab. The temperature of the medium was chosen to be  $T = 10\text{K}$ , since in this regime the analytical expression is accurate for optical depths down to  $\tau_0 \sim 10^4$ , which is faster to compute with the code.

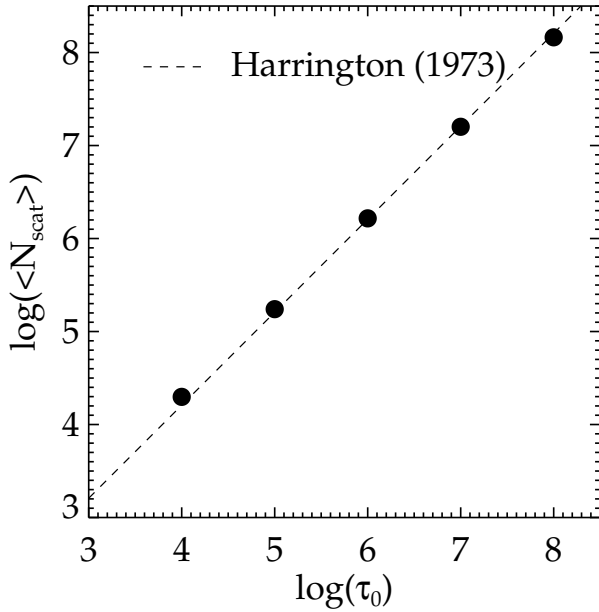


**Figure A3.** Mean number of scatterings as a function of the optical depth in the line centre of the medium. The circles show the results from the Monte Carlo code for configurations with different  $\tau_0$ . The dashed line shows the analytical solution of Harrington (1973).

The typical Ly $\alpha$  line profile is double peaked, and is symmetrical with respect to the line centre. The centres of the peaks are displaced away from  $x = 0$  by a value determined by  $\tau_0$ . The higher the optical depth, the farther away from the line centre and the wider the profile will be. Fig. A2 compares the analytic solution of Harrington (1973) with the output from the basic code (orange histogram), and the accelerated version (blue histogram). Overall, it is clear that the non-accelerated version of the code reproduces the analytical formula over the range of optical depths shown here. When  $x_{\text{crit}} = 3$  (the blue histogram in Fig. A2), the output is virtually indistinguishable from the non-accelerated version, but the running time has been decreased by a factor  $\sim 200$ . Therefore, Fig. A2 confirms that the choice of  $x_{\text{crit}} = 3$  does not compromise the accuracy of the results.

Harrington (1973) also computed the mean number of scatterings expected before a Ly $\alpha$  photon escapes from an optically thick medium for the homogeneous slab. He found

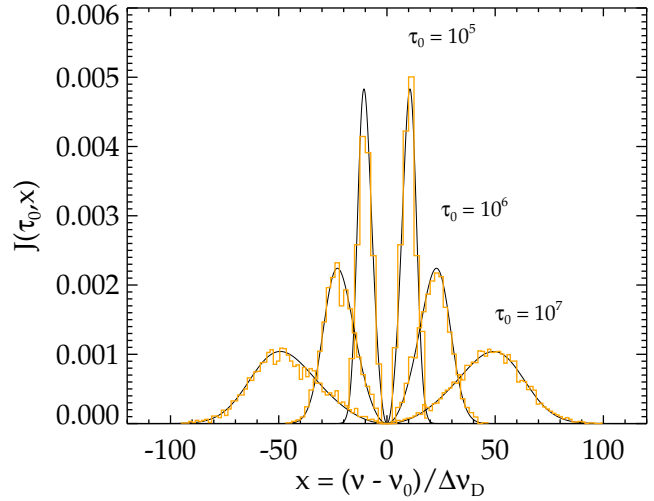
$$\langle N_{\text{scat}} \rangle = 1.612\tau_0. \quad (\text{A18})$$

Fig. A3 shows a comparison between the mean number of scatterings computed using our code with the analytical prediction of Harrington (1973). The agreement is remarkably good.

Following closely the methodology of Harrington (1973) and Neufeld (1990), Dijkstra, Haiman & Spaans (2006) computed the emergent spectrum from a static sphere. Fig. A4 shows a comparison between the analytic prediction and the output from the code at different optical depths. Again, there is a very good agreement between the two. The optical depths shown in Fig. A4 were chosen to be different from those in Fig. A2 to show that the code is following closely the expected emergent spectrum for a range of optical depths spanning several orders of magnitude.

Neufeld (1990) computed an analytical expression for the escape fraction of photons emitted from an homogeneous, dusty slab.

Fig. A5 shows a comparison between the escape fraction obtained from a series of simulations, keeping  $\tau_0$  fixed and varying



**Figure A4.** Ly $\alpha$  spectrum emerging from a homogeneous static sphere at  $T = 10\text{K}$ , for optical depths at the line centre of  $\tau_0 = 10^5, 10^6$  and  $10^7$ . The profiles are symmetric around  $x = 0$ . The thicker the medium, the farther from the line centre the resulting peaks of each profile are found. The solid lines show the analytical solution of Dijkstra, Haiman & Spaans (2006) and the histograms show the results from our Monte Carlo code.

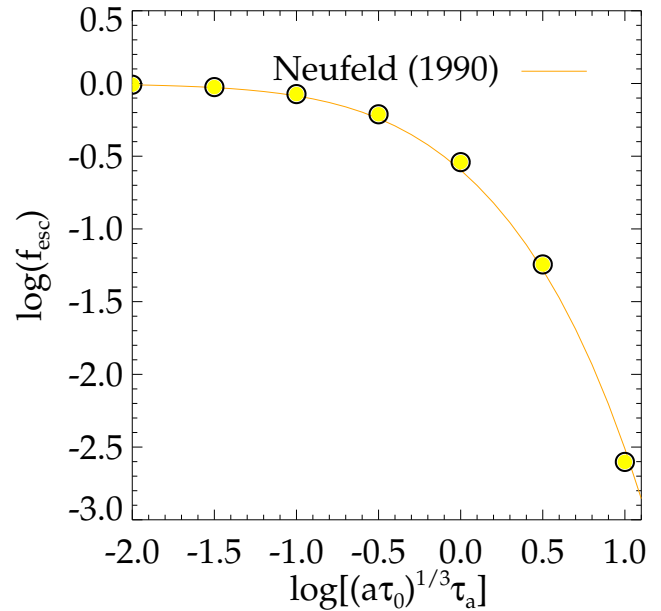


**Figure A5.** The escape fraction of Ly $\alpha$  photons from an homogeneous dusty slab. The optical depth of hydrogen scatterings at the line centre  $\tau_0$  is held constant at  $\tau_0 = 10^6$ , and different values of the optical depth of absorption  $\tau_a$  are chosen. Circles show the output from the code, and the solid orange curve shows the analytical prediction of Neufeld (1990).

$\tau_a$ , with the analytical solution of Neufeld (1990). We find a remarkable agreement between the analytical solution and our code. The escape fraction, as expected, decreases rapidly for increasing  $\tau_a$ , which, for a fixed  $\tau_0$ , translates into having a higher concentration of dust in the slab.

To validate the effect of bulk motions in the gas, we model the case of an expanding homogeneous sphere, with a velocity at a

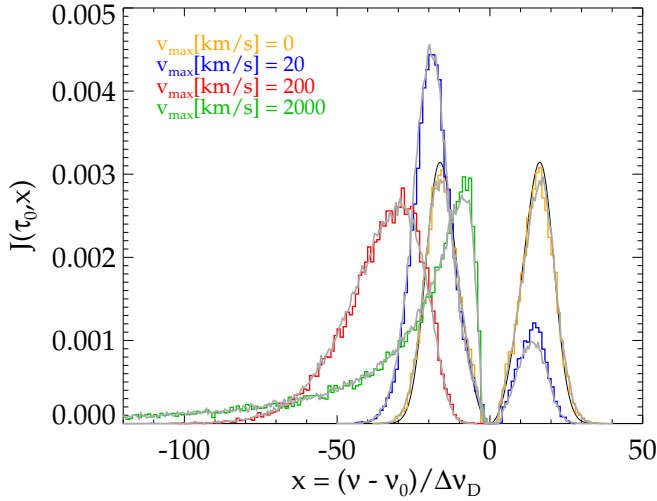


**Figure A6.** The emergent Ly $\alpha$  spectrum from a linearly expanding sphere with velocity zero at the centre and velocity at the edge  $v_{max} = 0, 20, 200$  and  $2000$  km/s shown in orange, blue, red and green respectively. The optical depth at the line centre is kept fixed at  $\tau_0 = 10^{7.06}$ . The analytical solution of Dijkstra, Haiman & Spaans (2006) for the static case is shown in black. The coloured histograms show the output from the code. The gray solid curves show the results obtained with the Laursen, Razoumov & Sommer-Larsen (2009) code MoCaLaTA (their Fig. 8).

distance  $r$  from the centre given by

$$v_{bulk} = Hr, \quad (A19)$$

$$H = \frac{v_{max}}{R}, \quad (A20)$$

where  $v_{max}$  is the velocity of the sphere at its edge, and  $R$  is the radius of the sphere.

There is no analytical solution for this configuration (except when  $T = 0$ , see Loeb & Rybicki (1999)), so we decided to compare our results to those found by a similar Monte Carlo code. We perform this comparison with media at  $T = 10^4$  K. Fig. A6 shows a comparison between our code and the results obtained with the MoCaLaTA Monte Carlo code (Laursen, Razoumov & Sommer-Larsen 2009). Both codes agree very well. Moreover, the figure helps us understand the effect of bulk motions of the gas on the emergent spectrum. First, when  $v_{max} = 0$  we recover the static solution, (Dijkstra, Haiman & Spaans 2006). When  $v_{max} = 20$  km/s, the velocity of the medium causes photons to have a higher probability of being scattered by atoms with velocities dominated by the velocity of the medium. These atoms *see* the photons as being redshifted, and hence the peak of the spectrum is shifted slightly towards the red part of the spectrum, although still a fraction of photons appear to escape blueshifted. When  $v_{max} = 200$  km/s, the blue peak is completely erased, and the peak is shifted even further to the red side. For very high velocities, such as  $v_{max} = 2000$  km/s, the velocity gradient makes the medium optically thin, and the average number of scatterings decreases drastically, and consequentially the photons have less chance of being redshifted far into the wings, thus shifting the peak back to the centre, but still with no photons in the blue side of the spectrum.

## APPENDIX B: THE EFFECT OF THE UV BACKGROUND

An additional feature of the Wind geometry is the option of computing the resulting ionization of the medium by photons in the intergalactic UV background. The Wind geometry, as described in detail in section 2.3.2, is assumed to be completely neutral, but photoionization from the UV background could have the effect of modifying the density profile of the neutral gas.

It is generally believed that the extragalactic UV background is dominated by radiation from quasars and massive young stars in star forming galaxies (Haardt & Madau 1996, 2001; Meiksin 2009). The mean intensity of the UV background at the observed frequency  $\nu_0$  and redshift  $z_0$  is defined as

$$J_0(\nu_0, z_0) = \frac{1}{4\pi} \int_{z_0}^{\infty} dz \frac{dl}{dz} \frac{(1+z_0)^3}{(1+z)^3} \epsilon(\nu, z) e^{-\tau_{eff}(\nu_0, z_0, z)}, \quad (B1)$$

where  $z$  is the redshift of emission,  $\nu = \nu_0(1+z)/(1+z_0)$ ,  $dl/dz$  is the line element in a Friedmann cosmology,  $\epsilon$  is the proper space-averaged volume emissivity and  $\tau_{eff}$  is an effective optical depth due to absorption by the IGM. There is no explicit solution of equation (B1) since it must be computed iteratively by solving the cosmological radiative transfer equation (Peebles 1993). For our analysis we use the values of  $J_0(\nu, z)$  tabulated by Haardt & Madau (2001). Notice, however, that more recent calculations of the UV background flux (Bolton & Haehnelt 2007; Meiksin 2009) show that the photoionizing background predicted by the Haardt & Madau (2001) model may be an underestimate at  $z > 5$ .

The fraction of ionized hydrogen  $x \equiv n_{HII}/n_H$  varies according to a balance between radiative and collisional ionizations and recombinations inside the cloud:

$$\alpha_A n_e x = (\Gamma_H + \beta_H n_e)(1-x), \quad (B2)$$

where  $\alpha_A = 4.18 \times 10^{-13} [\text{cm}^3 \text{s}^{-1}]$  is the case A recombination coefficient at  $T = 10^4$  K (Osterbrock 1989), the photoionization rate  $\Gamma_H(z)$  from the UV background is given by

$$\Gamma_H(z) = \int_{\nu_0}^{\infty} \frac{4\pi J_0(\nu, z)}{h\nu} \sigma_{\nu}(H) d\nu, \quad (B3)$$

and the collisional ionization rate at  $T = 10^4$  K, is  $\beta_H = 6.22 \times 10^{-16} [\text{cm}^3 \text{s}^{-1}]$  (Cen 1992).

As the UV flux penetrates the outflow, it will be attenuated by the outer layers of neutral hydrogen. The UV flux reaching an inner layer of the HI region is attenuated by this *self-shielding* process according to

$$J(\nu) = J_0(\nu) e^{-\tau(\nu)}, \quad (B4)$$

where  $J_0(\nu)$  is the original, un-shielded UV flux, and the optical depth  $\tau(\nu)$  when UV photons travel a distance  $d$  inside the HI region (coming from outside) is given by

$$\tau(\nu) = \sigma_{\nu}(H) \int_{R_{out}}^d n_H(r) dr. \quad (B5)$$

The photoionization rate is computed from the outer radius inwards. For each shell inside the outflow,  $\Gamma_H$  is computed taking into account the attenuation given by equations (B4) and (B5), making the photoionization rate smaller as photons penetrate inside the HI region.

We have found that the result of this calculation modifies strongly the outer layers of the wind, but since the number density of atoms increase rapidly when going inwards, the self-shielding effect effectively suppresses the UV radiation for the inner layers



of the wind. For winds with low neutral hydrogen column densities the UV background is found to penetrate deeper into the wind, but in general the innermost region is left unchanged.

In principle, we could compute the effect of the UV background on the Shell geometry as well. However, we do not perform this calculation since, in this case, the number density inside the outflow layers depend strongly on the physical thickness of the Shell, which in turn depends on the parameter  $f_{th}$ . As discussed in the previous section, this parameter is considered to have an arbitrary value provided that  $f_{th} \gtrsim 0.9$ . If we include the UV background in the Shell geometry, the  $\text{Ly}\alpha$  properties would depend on the value of  $f_{th}$  assumed, which is an unnecessary complication to the model.

### APPENDIX C: A GRID OF CONFIGURATIONS TO COMPUTE THE ESCAPE FRACTION

GALFORM typically generates samples numbering many thousands of galaxies brighter than a given flux limit at a number of redshifts. The task of running the radiative transfer code for each galaxy is infeasible considering the time it takes the Monte Carlo code to reach completion, which varies from a few seconds up to several hours for some extreme configurations. Therefore, this motivates the need to develop an alternative method to assign a  $\text{Ly}\alpha$  escape fraction for each galaxy predicted by GALFORM. Instead of running the radiative transfer code to each galaxy, we construct a grid of configurations spanning the whole range of galaxy properties, as predicted by GALFORM.

The first step to construct the grid is to choose which parameters will be used. In principle, each outflow geometry (Wind or Shell) requires 4 input parameters from GALFORM: three of these,  $\langle V_{\text{circ}} \rangle$ ,  $\langle R_{1/2} \rangle$  and  $\langle Z_{\text{gas}} \rangle$  are used by both geometries. In addition,  $\dot{M}_{ej}$  is required in the Wind geometry, and  $\langle M_{\text{gas}} \rangle$  in the Shell geometry.

However, a grid of models using four parameters becomes rapidly inefficient when trying to refine the grid. A grid with an appropriate binning of each parameter can have as many elements as the number of galaxies for which the grid was constructed, and hence also becomes prohibitively expensive.

Therefore, we look for degeneracies in the escape fraction when using combinations of the input parameters from GALFORM, in order to reduce the number of parameters for the construction of the grid. The idea is to find a combination of parameters which, when kept fixed while varying its individual components, gives the same escape fraction.

The natural choice for this is to use the column density  $N_H$  as one parameter. Neufeld (1990) found that the escape fraction from a homogeneous, dusty slab is a function of the optical depth at the line centre  $\tau_0$  and the optical depth of absorption  $\tau_a$ . Both quantities are, in turn, a function of the column density  $N_H$ . In the Shell geometry,  $N_H \propto M_{\text{gas}} / \langle R_{1/2} \rangle^2$ , whereas in the Wind geometry  $N_H \propto \dot{M}_{ej} / (\langle R_{1/2} \rangle V_{\text{exp}})$ . Although promising, we find that we do not recover a constant escape fraction in the Wind geometry when the column density is kept fixed while varying its individual terms. The reason is that the expansion velocity plays a more complicated role when computing the escape fraction, with the escape fraction increasing rapidly with increasing velocity regardless of the other parameters of the medium.

Therefore, we construct three-dimensional grids for each outflow geometry. We define  $C_{\text{wind}} \equiv \dot{M}_{ej} / R_{\text{inn}}$ , and  $C_{\text{shell}} \equiv M_{\text{shell}} / R_{\text{shell}}^2$ . Then, in the Wind geometry the parameters are

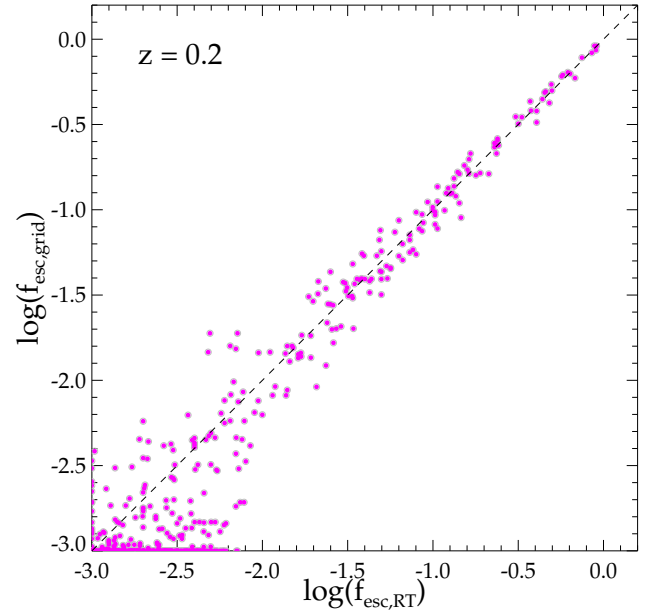


**Figure C1.** Comparison of the escape fraction obtained using a direct calculation ( $f_{\text{esc,RT}}$ ) or interpolating from a grid ( $f_{\text{esc,grid}}$ ). Points represent a subsample of  $\sim 1000$  galaxies selected from GALFORM at  $z = 0.2$ .

$C_{\text{wind}}$ ,  $V_{\text{exp}}$  and  $Z_{\text{gas}}$ , whereas in the Shell geometry we use  $C_{\text{shell}}$ ,  $V_{\text{exp}}$  and  $Z_{\text{gas}}$ . We choose to cover each parameter with a bin size appropriate to recover the expected escape fraction with a reasonable accuracy when interpolating in the grid, but also ensuring that the number of grid elements to be computed is significantly smaller than the total number of galaxies in the sample.

We find that, when covering each parameter in logarithmic bins of 0.1 we get escape fractions that are accurate enough, and the number of elements of the grid we need to compute is usually a factor  $\sim 20$  smaller than the total number of galaxies in the sample.

We fix the number of photons to run for each grid point to compute the escape fraction, since this will determine the speed with which each configuration will be completed. By studying the resulting luminosity function of galaxies, we find that running the code with a maximum number of photons  $N_p = 1000$  gives results which have converged over the range of luminosities observed. This means that the minimum escape fraction we are able to compute is  $f_{\text{esc}} = 10^{-3}$ . Although there are configurations where  $f_{\text{esc}}$  can be lower than this, they are found not to contribute significantly to the luminosity functions.

Fig. C1 shows an example of the performance of the grid we use to compute the escape fraction in the Shell geometry using a sub-sample of galaxies from GALFORM at  $z = 0.2$ , chosen in a way to cover the entire range of intrinsic  $\text{Ly}\alpha$  luminosities. The accuracy of the grid gets progressively worse with lower escape fractions, since these have intrinsically larger errors due to the constraint on the maximum number of photons used to compute  $f_{\text{esc}}$ . However, as discussed previously, we found that to reproduce accurately the luminosity functions there is no need to reduce the size of the parameter bins or increase the number of photons used.